Inorganic Chemistry

pubs.acs.org/IC Article

Azide-Coordination in Homometallic Dinuclear Lanthanide(III) Complexes Containing Nonequivalent Lanthanide Metal Ions: Zero-Field SMM Behavior in the Dysprosium Analogue

Pawan Kumar, Sourav Biswas, Abinash Swain, Joydev Acharya, Vierandra Kumar, Pankaj Kalita, Jessica Flores Gonzalez, Olivier Cador, Fabrice Pointillart,* Gopalan Rajaraman,* and Vadapalli Chandrasekhar*

Cite This: *Inorg. Chem.* 2021, 60, 8530−8545

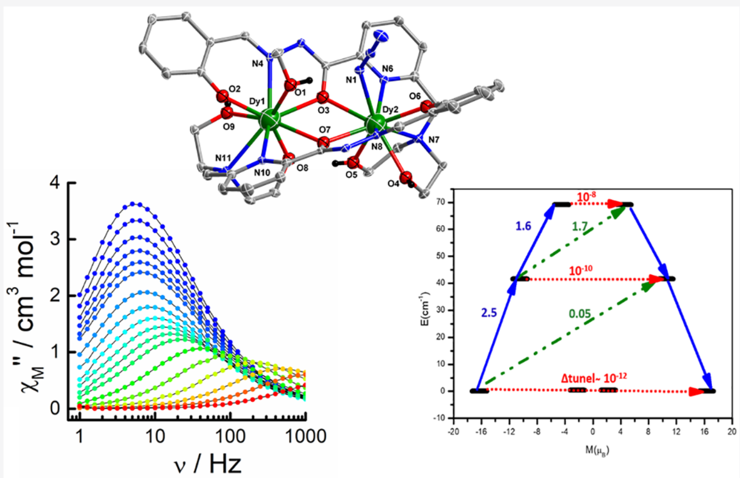

ABSTRACT: A series of homometallic dinuclear lanthanide complexes containing nonequivalent lanthanide metal centers $[Ln_2(LH_2)(LH)(CH_3OH)(N_3)]\cdot x\text{MeOH}\cdot yH_2O$ [**1**, Ln = Dy^{III}, $x = 0$, $y = 2$; **2**, Ln = Tb^{III}, $x = 1$, $y = 1$] have been synthesized [LH_4 = 6-((bis(2-hydroxyethyl)amino)-*N*′-(2-hydroxybenzylidene)picolinohydrazide] and characterized. The dinuclear assembly contains two different types of nine-coordinated lanthanide centers, because the nonequivalent binding of the azide co-ligand as well as the varying coordination of the deprotonated Schiff base ligand. Detailed magnetic studies have been performed on the complexes **1** and **2**. Complex **1** and its diluted analogue ($\mathbf{1}_{5\%}$) are zero-field SMMs with effective energy barriers (U_{eff}) of magnetization reversal equal to 59(3) K and 66(3) K and relaxation times of $\tau_0 = 10(4) \times 10^{-6}$ s and $10(4) \times 10^{-8}$ s, respectively. On the other hand, complex **2** shows a field-induced SMM behavior. Combined *ab initio* and density functional theory calculations were performed to explain the experimental findings and to unravel the nature of the magnetic anisotropy, exchange-coupled spectra, and magnetic exchange interactions between the two lanthanide centers.

■ INTRODUCTION

Single-molecule magnets (SMMs) are discrete molecular complexes comprising 3d/4d/5d/4f/5f metal ions or a combination thereof, such as 3d/4f heterometallic complexes, which can be magnetized upon application of a magnetic field and retain their magnetization below a certain temperature (known as the blocking temperature, T_B).[1] These systems show slow relaxation of magnetization, which depends on an energy barrier (U_{eff}) for the magnetization reversal.[2] For molecules to display SMM behavior, there is a requirement of a large ground spin state (S) and an Ising-type anisotropy. Among the various types of complexes investigated, complexes containing lanthanide metal ions are most promising, because of these having a large ground-state single-ion magnetic anisotropy, which results from a very high spin−orbit coupling. In addition many lanthanide ions such as Dy^{III} and Tb^{III} have a reasonable ground state spin, because of the presence of a sufficient number of unpaired electrons.[3] The investigations on

Received: January 26, 2021
Published: June 4, 2021

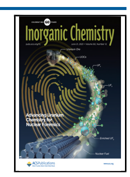

Table 1. Crystal Data and Structure Refinement Parameters of 1, 1_Y, and 2

	1	1_Y	2
formula	$C_{37}H_{43}Dy_2N_{11}O_9$	$C_{37}H_{43}Y_2N_{11}O_9$	$C_{37}H_{43}N_{11}O_9Tb_2$
g/mol	1110.82	963.64	1139.69
crystal system	monoclinic	monoclinic	monoclinic
space group	$C2/c$	$C2/c$	$C2/c$
a/Å	25.561(11)	25.494(7)	25.519(14)
b/Å	16.456(11)	16.411(4)	16.432(14)
c/Å	22.709(11)	22.618(6)	22.762(14)
α (deg)	90	90	90
β (deg)	90.605(2)	90.366(2)	90.779(10)
γ (deg)	90	90	90
V/Å^3	9552.4(9)	9463.6(4)	9544.6(11)
Z	8	8	8
ρ_c/g cm^{-3}	1.545	1.353	1.586
μ/mm^{-1}	3.162	2.499	3.003
F(000)	4368.0	3936.0	4512.0
cryst size (mm^3)	0.24 × 0.15 × 0.13	0.11 × 0.1 × 0.08	0.24 × 0.16 × 0.012
2θ range (deg)	4.628−56.518	5.28−57.92	5.662−56.616
limiting indices	$-34 \leq h \leq 34$	$-33 \leq h \leq 32$	$-34 \leq h \leq 34$
	$-21 \leq k \leq 21$	$-16 \leq k \leq 22$	$-21 \leq k \leq 21$
	$-30 \leq l \leq 30$	$-30 \leq l \leq 30$	$-30 \leq l \leq 30$
reflns collected	75597	78591	100713
ind reflns	11815 [R(int) = 0.0507]	11502 [R(int) = 0.0681]	11827 [R(int) = 0.0417]
completeness to θ (%)	100	100	100
refinement method	full-matrix least-squares on F^2	full-matrix least-squares on F^2	full-matrix least-squares on F^2
data/restraints/params	11815/0/547	11502/12/545	11827/12/545
goodness-of-fit on F^2	1.029	1.033	1.060
Final R indices [$I > 2\theta(I)$]	R_1 = 0.0218	R_1 = 0.0495	R_1 = 0.0227
	wR_2 = 0.0505	wR_2 = 0.1148	wR_2 = 0.0547
R indices (all data)	R_1 = 0.0286	R_1 = 0.0668	R_1 = 0.0265
	wR_2 = 0.0532	wR_2 = 0.1197	wR_2 = 0.0562
CCDC no.	2026262	2058082	2026261

lanthanide complexes as SMMs began with Isikawa's seminal discovery of slow relaxation of magnetization in the sandwich complex $[Bu_4N][TbPc_2]$.[4] It was quickly realized that lanthanide ions with their intrinsic unquenched orbital angular momenta could contribute to magnetic anisotropy. In recent years, a large number of lanthanide-based SMMs with very high effective energy barriers of magnetization above 1000 K[5] and blocking temperatures up to 80 K[6] have been reported. While the mononuclear Dy^{III} complexes yielded very attractive blocking temperatures in recent years, the axial limit set by the ligand field has already been breached for mononuclear complexes. Therefore, expanding the structural motif beyond monomers is important.[7] Among these systems, dinuclear complexes are of interest because these allow an understanding of the interactions between the two lanthanide ions.[8] The magnetic coupling between the lanthanide ions can generate an exchange bias field that could minimize the quantum tunneling of the magnetization.[9] Among such dinuclear complexes, those containing nonequivalent lanthanide ions are especially sparse.[8a,10]

We have been involved in the design of polydentate ligands for assembling various types of lanthanide complexes whose nuclearity varied from 1 to 21.[11] In these efforts, we found, similar to some other groups, that aroylhydrazone-based Schiff base ligands are particularly efficient in the construction of lanthanide complexes.[12] We have synthesized a pyridine-based Schiff base ligand (LH_4) and utilized it for preparing lanthanide complexes. Furthermore, we were also interested in incorporating the azide ligand in the assembly of these complexes in view of its demonstrated coordination motif versatility in transition-metal complexes.[13] Although we anticipated a bridging coordination action from the azide ligand, as discussed below, we observe that this ligand binds in a monodentate fashion as a terminal ligand. Accordingly, herein, we report the synthesis, structural characterization and magnetic studies of $[Ln_2(LH_2)(LH)(CH_3OH)(N_3)]\cdot x$MeOH$\cdot y H_2O$ [**1**, Ln = Dy^{III}, $x = 0$, $y = 2$; **2**, Ln = Tb^{III}, $x = 1$, $y = 1$]. Although we have prepared the Gd(III) analogue (**3**), we were unable to establish the bulk purity of this compound. However, we were able to get single crystals in some quantity. We could perform the structural study, which are presented in the Supporting Information. Among these complexes, the Dy^{III} analogue is a zero-field SMM. Also, while the Dy^{III} analogue has been shown to have antiferromagnetic interaction between the two Dy^{III} centers, the Tb^{III} analogue has been shown to possess ferromagnetic interactions. These conclusions were possible by a theoretical study of the Gd^{III} analogue. The differences between the Dy^{III} and Tb^{III} derivatives could be correlated to small structural changes in these complexes. All of these aspects are discussed herein through combined experimental and *ab initio* theoretical calculations.

■ EXPERIMENTAL SECTION

Solvents and other general reagents used in this work were purified according to standard procedures.[14] Pyridine-2,6-dicarboxylic acid, sodium borohydride, sodium azide, $DyCl_3\cdot 6H_2O$, $TbCl_3\cdot 6H_2O$, $YCl_3\cdot$

https://doi.org/10.1021/acs.inorgchem.1c00249
Inorg. Chem. 2021, 60, 8530−8545

$6H_2O$, and $GdCl_3{\cdot}6H_2O$ were obtained from Sigma−Aldrich Chemical Co. and were used as received. Diethanolamine, hydrazine hydrate (80%), PBr_3, and sodium sulfate (anhydrous) were obtained from SD. Fine Chemicals, Mumbai, India. Methyl-6-(hydroxymethyl) picolinate,[15] methyl 6-(bromomethyl)picolinate,[15] methyl-6-((bis(2-hydroxyethyl)amine)methyl)picolinate,[11d] and 6-((bis(2-hydroxyethyl)amino)methyl)picolinohydrazide (A_5),[11d] were prepared according to literature procedure.

Instrumentation. Melting points were measured using a JSGW melting point apparatus and are uncorrected. IR spectra were recorded as KBr pellets on a Bruker Vector 22 FT IR spectrophotometer operating at 400−4000 cm^{-1}. Elemental analyses of the compounds were obtained from Thermoquest CE instruments CHNS-O, EA/110 model. ESI-MS spectra were recorded on a Micromass Quattro II triple quadrupole mass spectrometer. ^1H NMR spectra were recorded in $CDCl_3$ and DMSO-d^6 solutions on a JEOL JNM Lambda 400 model spectrometer operating at 500.0 MHz, Chemical shifts are reported in parts per million (ppm) and are referenced with respect to internal tetramethylsilane (^1H). A powder X-ray diffraction (XRD) study was done on **1** and **2** with a Bruker D8 Avance powder XRD diffractometer. The samples for study were prepared by finely grinding the crystals of **1** and **2** to powder form.

X-ray Crystallography. Single-crystal data for the complexes were collected on a Bruker *SMART* CCD diffractometer (Mo Kα radiation, λ = 0.71073 Å). The program *SMART*[16] was used for collecting frames of data, indexing reflections, and determining lattice parameters, *SAINT* for integration of the intensity of reflections and scaling, *SADABS*[17] for absorption correction, and *SHELXTL*[18] for space group and structure determination and least-squares refinements on F^2. On the other hand, XRD data for complex $\mathbf{1_Y}$ was collected at low temperature (120 K) by using Rigaku diffractometer with graphite-monochromated Mo Kα radiation, λ = 0.71073 Å. Data integration and reduction were processed with CrysAlisPro software.[19] An empirical absorption correction was applied to the collected reflections with SCALE3 ABSPACK integrated with CrysAlisPro. The crystal structures were solved and refined by full-matrix least-squares methods against F^2 by using the program *SHELXL-2014*,[20] using *Olex-2*[21] software. All the non-hydrogen atoms were refined with anisotropic displacement parameters. Hydrogen positions were fixed at calculated positions and refined isotropically. The crystallographic figures have been generated using *Diamond 3.1e* software.[22] In addition, some disorderd solvent molecules was present in complexes **1** and **2**. We could not assign all the solvent molecules properly due to the disorder and weak residual Q peaks. So the Olex-2 mask program was utilized to discard the disordered solvents molecules which give an electron density of ~18 and 26, corresponding to the presence of two water molecules in **1** and one methanol molecule and one water molecule in **2**, respectively. The possible masked electron counts and void volumes has been included in the corresponding CIFs.

The crystal data, the cell parameters and ccdc information for all the complexes are summarized in Table 1 and Table S1 in the Supporting Information.

Magnetic Measurements. The dc magnetic susceptibility measurements were performed on solid polycrystalline samples with a Quantum Design MPMS-XL SQUID magnetometer between 2 and 300 K in applied magnetic field of 200 Oe for temperatures between 2 and 20 K, 2 kOe between 20 K and 80 K, and 10 kOe at >80 K. The sample was immobilized in a pellet made with Teflon tape. These measurements were all corrected for the diamagnetic contribution as calculated with Pascal's constants. The ac magnetic susceptibility measurements were performed on Quantum Design MPMS-XL SQUID magnetometer in the frequency range of 1−1000 Hz.

Computational Details. The *ab initio* calculations have been performed using MOLCAS 8.2 software package using CASSCF/RASSI-SO/SINGLE_ANISO module.[23] For POLY_ANISO simulations, the inputs were taken from the SINGLE_ANISO results.[24] In the CASSCF step for Dy^{III} complex, nine electrons in seven 4f active orbitals and for Tb^{III} complex eight electrons in seven 4f orbitals were taken into consideration. For **1** 21 sextets and for **2** 7 septets, 140 doublets and 195 quartet roots were taken into consideration in the RASSI-SO step, as established earlier by us and others.[25] The basis sets are of ANO-RCC···8s7p4d3f2g1h TZVP level for the paramagnetic center Ln^{III} and Lu^{III}, ANO-RCC···8s7p4d3f2g1h TZV quality for O and N atoms, since they are coordinating to the metal ion and ANO-RCC···3s2p/ANO-RCC···2s DZV level for the rest of the atoms. The relativistic effect was taken care of by taking DKH Hamiltonian. In order to save disk space, Cholesky decomposition has been incorporated for our calculations.[23a] Spin−orbit coupling was taken into account through the RASSI-SO module using the CASSCF functions as input states. From the SINGLE-ANISO computation, the *g* tensor for the ground state and excited state, magnetic susceptibility, crystal field parameter and orientation of main magnetic axes have been obtained.[26] Lines model was employed to calculate the exchange interaction between two Ln^{III} sites using POLY-ANISO program.[27] The experimentally obtained susceptibility values were simulated with the POLY_ANISO module/program to get the exchange interaction between the two Ln^{III} centers for both **1** and **2**.

The exchange values obtained through this method was further verified by density functional calculations using the Gaussian 09 program employing the DFT broken symmetry approach.[28] For this approach, we have used the B3LYP hybrid functional, with Cundari−Stevens (CS) relativistic effective core potential for Gd atom and TZV level of basis set for the rest of the atoms.[29] Quadratic convergence method was followed to the most stable wave function. Since the Dy^{III} and Tb^{III} ion are highly anisotropic paramagnetic systems, to reduce the complexity in using DFT methods, we have replaced the Dy^{III} and Tb^{III} ion in the corresponding X-ray structure with Gd^{III} ion and computed the *J*s using the DFT method and rescaled the *J* values later, using appropriate spin to get the exchange values.[30] By this approach, the difference in structural parameters, however small, can be captured in the estimation of *J* values. Also, this being an independent method offers the possibility to cross-verify results obtained using the Lines model wherein the experimental susceptibility data is fit to the ab initio computed parameters to extract the *J* values. The exchange values for Dy^{III}/Tb^{III} has been calculated by multiplying 5/7 and 6/7 with the exchange values obtained from DFT using Gd^{III} ion. For the Gd(III) analogue, the exchange values were estimated by the use of broken symmetry calculation using ORCA 4.2 package. For this, TZVP level was used for Gd, and for the rest of the atoms, def2-SVP has been used.

Synthesis. Compounds A_1−A_5 (Scheme S1 in the Supporting Information) were prepared according to literature procedures.[11d,15]

6-((Bis(2-hydroxyethyl)amino)methyl)-*N*′-(2-hydroxybenzylidene)picolinohydrazide (LH_4). Salicylaldehyde (A_6) (0.19g, 1.6 mmol) was added to a solution of 6-((bis(2-hydroxyethyl)amino)methyl)picolinohydrazide (A_5) (0.406 g, 0.0016 mol) in ethanol with stirring. The reaction mixture was refluxed for 6 h, cooled, and the solvent reduced in vacuo. The concentrated solution was kept in a refrigerator affording a white precipitate which was washed with diethyl ether and dried. This was shown to be 6-((bis(2-hydroxyethyl)amino)methyl)-*N*′-(2-hydroxybenzylidene)-picolinohydrazide (LH_4) (0.305, 76%). Anal. Calcd For $C_{18}H_{22}N_4O_4$ (358.40): C, 60.32; H, 6.19; N, 15.63. Found: C, 60.58; H, 5.99; N, 15.52. Mp: 164 °C.

^1H NMR (400 MHz, DMSO-d_6) 12.12 (s,1H,N*H*), 11.36 (s,1H,Ph-O*H*), 8.86 (s,1H,C*H*), 8.04 (m,2H,Py-*H*), δ = 7.84-(d,1H,Py-*H*), 7.52 (d,1H,Ph-*H*), 7.32 (t,1H,Ph-*H*), 6.94 (m,2H,Ph-*H*), 4.47 (br,2H,O*H*) 3.95 (s,2H,CH_2), 3.50 (t,4H,CH_2), 2.65 (t,4H,CH_2), IR (KBr) cm^{-1}: 3498 (br), 3443 (br), 3176 (br), 2955 (s), 2880 (br), 2804 (s), 1675 (s), 1622 (s), 1594 (w), 1536 (s), 1491 (w), 1474 (w), 1449 (s), 1398 (w), 1380 (s), 1371 (w), 1273 (s), 1244 (w), 1222 (w), 1169 (w), 1154 (s), 1045 (s), 971 (s), 898 (s), 780 (w), 737 (s), 698 (w), 678 (s), 566 (w), 518 (s). ESI-MS *m*/*z*, ion: 359.1701, $(C_{18}H_{23}N_4O_4)^+$.

General Synthetic Procedure for the Preparation of the Complexes 1 and 2. To a stirred solution of LH_4 (0.040 g, 0.11 mmol), in methanol (30 mL), $LnCl_3{\cdot}6H_2O$ (0.11 mmol) was added to give a yellow-colored solution, which was allowed to stir for 10 min at room temperature. Then, NaN_3 (0.010 g, 0.15 mmol) was added,

https://doi.org/10.1021/acs.inorgchem.1c00249
Inorg. Chem. 2021, 60, 8530−8545

Scheme 1. LH_4 Showing Unsymmetrical Coordination Pockets, Various Conformations Based on Base-Assisted Reversible Keto-Enol Tautomerization and Coordination Modes

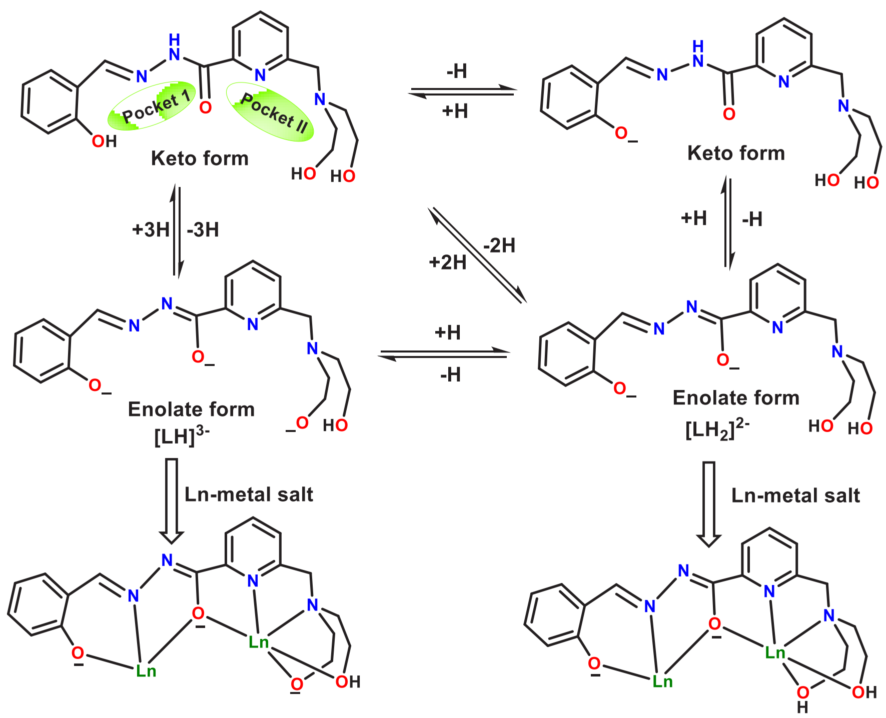

followed by the addition of triethylamine (0.046 mL, 0.33 mmol). The reaction mixture was allowed to stir for 6−8 h at room temperature. The reaction mixture was filtered and stripped off its solvent in vacuo affording a semisolid yellow residue, which was dissolved in methanol containing a few drops of chloroform. Suitable crystals for XRD were obtained by slow evaporation of the solvents within a week. A similar synthetic method was employed for the preparation of the yttrium analogue, the diluted analogue of complex **1** ($\mathbf{1}_{5\%}$). Specific details of each reaction and the characterization data of the complexes are given below.

*[$Dy_2(LH_2)(LH)(CH_3OH)(N_3)$]·$2H_2O$ (**1**).* Quantities: LH_4 (0.040 g, 0.11 mmol), $DyCl_3$•$6H_2O$ (0.041 g, 0.11 mmol), NaN_3 (0.010 g, 0.15 mmol), Et_3N (0.046 mL, 0.33 mmol). Yield: 0.046 g, 74.07% (based on the Dy^{III} salt). Mp: > 250 °C (d). IR (KBr) cm^{-1}: 3373 (br), 2963 (br), 2848 (br), 2053.37(s), 2036(s), 1609 (s), 1571 (w), 1554 (s), 1536 (s), 1474 (s), 1442 (w), 1429, 1356 (s), 1263 (w), 1220 (w), 1198 (s), 1149 (s), 1080 (s), 1015 (s), 1010 (w), 883 (s), 850 (s), 796 (w), 759 (s), 709 (w), 691 (s), 595 (s), 532 (s). Anal. Calcd For C_{38} H_{47} Dy_2 N_{11} O_{10}(1142.86): C, 38.75; H, 4.13; N, 13.43 Found: C, 39.05; H, 4.55; N, 13.91. ESI-MS *m*/*z*, ion: 518.5698, $(C_{36}H_{40}Dy_2N_8O_8)^{2+}$.

[$Y_2(LH_2)(LH)(CH_3OH)(N_3)$]·$2H_2O$ ($\mathbf{1}_Y$). Quantities: LH_4 (0.040 g, 0.11 mmol), YCl_3•$6H_2O$ (0.0338 g, 0.11 mmol), NaN_3 (0.010 g, 0.15 mmol), Et_3N (0.046 mL, 0.33 mmol). Yield: 0.041 g, 73.74% IR (KBr) cm^{-1}: 3342 (br), 2036.35 (s), 1610.78 (s), 1571 (w), 1556.33 (s), 1475 (s), 1357.42 (s), 1199 (s), 1079 (s), 851 (s), 760 (s). Anal. Calcd For C_{37} H_{47} Y_2 N_{11} O_{11} (999.15): C, 44.76; H, 4.74; N, 15.41 Found: C, 45.17; H, 4.95; N, 15.89.

*5% Diluted Analogue of **1** ($\mathbf{1}_{5\%}$).* Quantities: LH_4 (0.040 g, 0.11 mmol), $DyCl_3$•$6H_2O$ (0.0021 g, 0.005 mmol), YCl_3•$6H_2O$ (0.0321 g, 0.105 mmol), NaN_3 (0.010 g, 0.15 mmol), Et_3N (0.046 mL, 0.33 mmol). IR (KBr) cm^{-1}: 3341 (br), 2854 (br), 2036.29(s),1610 (s), 1571 (w), 1536 (s), 1474 (s), 1444 (w), 1357 (s), 1263 (w), 1198 (s), 1149 (s), 1078 (s), 1015 (s), 851 (s), 759 (s).

*[$Tb_2(LH_2)(LH)(CH_3OH)(N_3)$]·$H_2O$·MeOH (**2**).* Quantities: LH_4 (0.040 g, 0.11 mmol), $TbCl_3$•$6H_2O$ (0.041 g, 0.11 mmol), NaN_3 (0.01 g, 0.15 mmol), Et_3N (0.046 mL, 0.33 mmol). Yield: 0.035 g, 55.2% (based on the Tb^{III} salt). Mp: > 250 °C (d). IR (KBr) cm^{-1}: 3342 (br), 2960 (br), 2909 (br), 2036 (s), 1610 (s), 1554 (w), 1536 (w), 1474 (s), 1442 (w), 1359 (s), 1262 (w), 1221 (w), 1198 (s), 1129 (w), 1078 (s), 1015 (s), 904 (w), 884 (w), 850 (s), 816 (w), 776 (w), 759 (s), 711 (w), 691 (w), 630 (w), 595 (w), 535 (s). Anal. Calcd For C_{38} H_{49} Tb_2 N_{11} O_{11} (1153.73): C, 39.56; H, 4.28; N, 13.35 Found: C, 39.97; H, 4.73; N, 13.89. ESI-MS *m*/*z*, ion: 515.0687, $(C_{36}H_{40}Tb_2N_8O_8)^{2+}$.

■ RESULTS AND DISCUSSION

Synthetic Aspects. Polyfunctional ligands have been used with a great deal of efficacy to assemble various complexes containing lanthanide ions. Among such multidentate ligands aroylhydrazone-based Schiff base ligands are particularly versatile, because of several features, including their flexibility involving C−C bond rotation and the potential of utilizing either the enolate or the keto forms of the ligand to bind to the metal ion.[11d,f,31] Harnessing these features, previously we have assembled dinuclear lanthanide complexes (Scheme S2 in the Supporting Information).[11d]

Motivated by the above results, we have designed and synthesized 6-((bis(2-hydroxyethyl)amino)-*N*′-(2-hydroxybenzylidene)picolinohydrazide (LH_4). The latter was prepared by following a five-step synthetic protocol (see Scheme S1 in the Supporting Information).

The ligand LH_4 contains seven coordination sites, which can be partitioned into two unsymmetrical pockets: a tridentate pocket consisting of a phenolic oxygen, an imine N, and hydrazine O (2O,1N), and the other is pentadentate, consisting of a pyridine N, a common hydrazone oxygen`and a diethanolamine motif (2N, 3O). The observed coordination behavior would be dependent also on the extent of deprotonation and can be summarized in the following way. If double deprotonation occurs the ligand would exist in the enol form, $[LH_2]^{2-}$. On the other hand, if triple deprotonation were to occur, where one arm of diethanolammine is deprotonated, $[LH]^{3-}$ (enol form) would result. In fact, in

https://doi.org/10.1021/acs.inorgchem.1c00249
Inorg. Chem. 2021, 60, 8530−8545

Scheme 2. Synthesis of Ln_2 Complexes 1−2

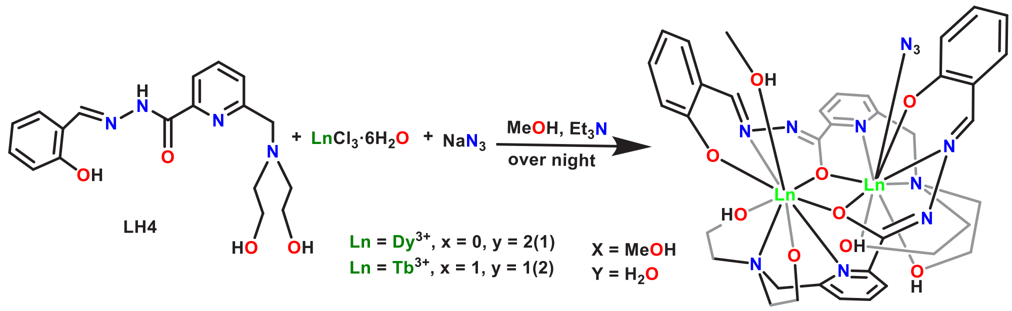

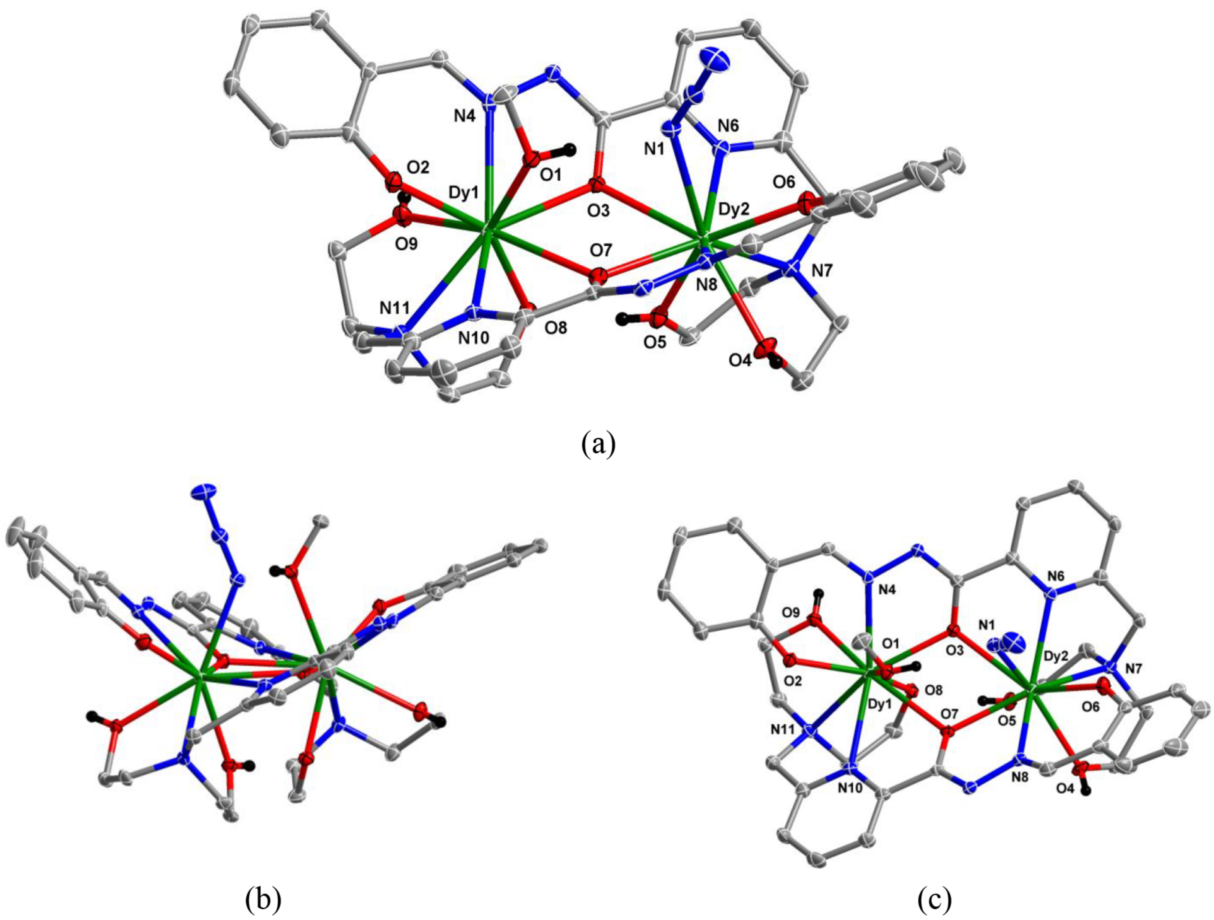

Figure 1. (a) Molecular structure of **1**, (b) side view of **1**, and (c) top view of **1**. Thermal ellipsoids at 50% probability level are shown (selected hydrogen atoms and the solvent molecules have been omitted for the sake of clarity). [Color codes: N = blue; O = red; C = gray; Dy = dark green, and H = black.]

the formation of the dinuclear complexes discussed herein, both $[LH_2]^{2-}$ and $[LH]^{3-}$ are involved (Scheme 1).

In addition to using the ligand LH_4, we have used sodium azide as the co-ligand with the intention of exploring the coordination capability of the azide ion. We anticipated a bridging coordination role for the azide ligand. However, as described below, because of the competing bridging coordination of the enolate form the ligand, the azide takes up a terminal position. Thus, the reaction of LH_4, $LnCl_3{\cdot}6H_2O$ and sodium azide in the presence of triethylamine in a molar ratio of 1:1:1:3 afforded dinuclear complexes, $[Ln_2(LH_2)(LH)(CH_3OH)(N_3)]{\cdot}x\text{MeOH}{\cdot}y\text{H}_2\text{O}$ [**1**, Ln = Dy^{III}, $x = 0$, $y = 2$; **2**, Ln = Tb^{III}, $x = 0$, $y = 2$] (see Scheme 2).

In order to check the phase purity of the complexes, powder XRD measurement for complexes was done and found that the sequence and pattern of the peaks are in reasonable agreement with the simulated data obtained from single-crystal data (see Figures S1 and S2 in the Supporting Information).

We have performed ESI-MS studies to check the structural integrity of these complexes in solution. These studies reveal peaks at m/z = 518.5698 and 515.0687 for **1**, **2** respectively, corresponding to the species $[Dy_2(LH_2)(LH)H]^{2+}$, $[Tb_2(LH_2)(LH)H]^{2+}$. This indicates that these complexes remain partially intact in solution. The ESI-MS spectra of complexes are given in the Supporting Information (see Figures S3 and S4 in the Supporting Information).

https://doi.org/10.1021/acs.inorgchem.1c00249
Inorg. Chem. 2021, 60, 8530−8545

Table 2. Selected Bond Distances and Bond Angles of 1

Bond Distances around Dy1		Bond Distances around Dy2		Bond Angles around Dy	
bond pair	distance (Å)	bond pair	distance (Å)	bond angle	value (°)
Dy(1)−O(7)	2.557(17)	Dy(2)−O(7)	2.341(17)	Dy(1)−O(3)−Dy(2)	115.80(7)
Dy(1)−O(8)	2.312(17)	Dy(2)−O(3)	2.516(17)	Dy(1)−O(7)−Dy(2)	114.87(7)
Dy(1)−O(3)	2.359(17)	Dy(2)−O(5)	2.376(19)		
Dy(1)−O(9)	2.526(19)	Dy(2)−O(4)	2.404(18)		
Dy(1)−O(2)	2.234(17)	Dy(2)−O(6)	2.217(18)		
Dy(1)−O(1)	2.492(19)	Dy(2)−N(6)	2.487(2)		
Dy(1)−N(11)	2.628(2)	Dy(2)−N(8)	2.516(2)		
Dy(1)−N(10)	2.525(2)	Dy(2)−N(7)	2.636(2)		
Dy(1)−N(4)	2.512(2)	Dy(2)−N(1)	2.544(2)		

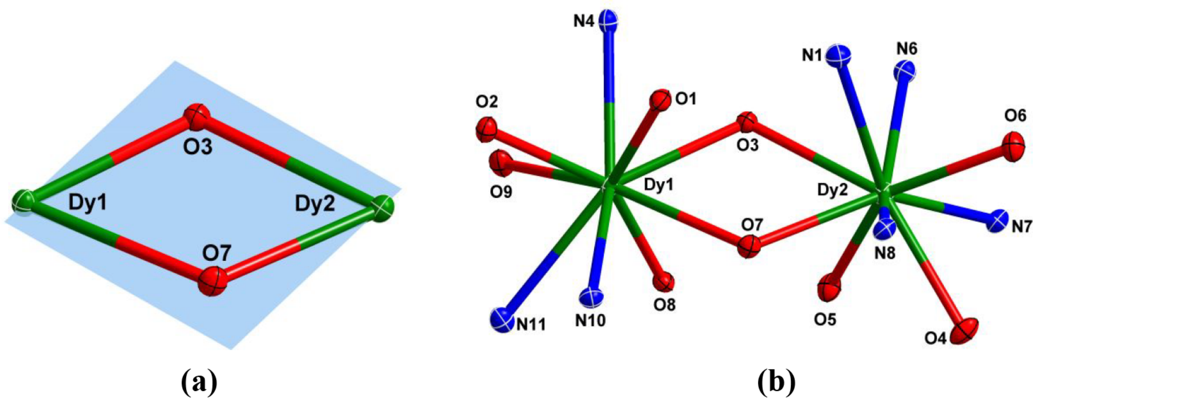

Figure 2. (a) Quadrilateral Dy_2O_2 core of 1; (b) core structure of 1. The outer backbone of the ligands are omitted for the sake of clarity.

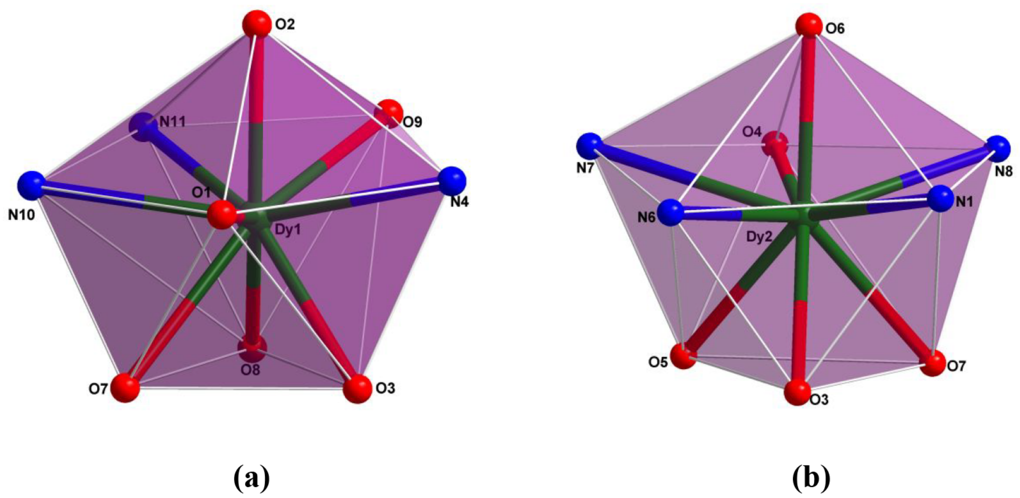

Figure 3. Spherical capped square antiprism coordination geometry around (a) Dy1 and (b) Dy2.

X-ray Crystallography. Suitable single crystals of the complexes 1−2 were obtained by slow evaporation of their solutions in methanol/chloroform mixture (1:1) within a week. Single-crystal XRD study reveals that the complexes 1−2 are isostructural and charge neutral. These crystallize in a monoclinic system ($C2/c$ with Z = 8). Since 1 and 2 are isostructural, we describe the molecular structure of 1 as a representative example. A perspective view of 1 is given in Figure 1 and that of complex 2 is given in the Supporting Information (see Figure S5 in the Supporting Information). Selected bond lengths and bond angles of 1 are given in Table 2, while those of 2 are given in Table S2 in the Supporting Information.

The molecular structure of 1 consists of two Dy^{III} ions, a dianionic ligand $[LH_2]^{2-}$, a trianionic ligand $[LH]^{3-}$, an azide anion, and a neutral methanol giving an overall neutral dinuclear assembly. Interestingly, the two lanthanide ions present in the assembly are nonequivalent as described below. The $[LH_2]^{2-}$ and $[LH]^{3-}$ ligands encapsulate the two Dy^{III} ions in a "head-to-tail" manner utilizing their two coordination pockets, a tridentate P1 (O, 2N) and a pentadentate P2 (3O, 2N) unit to generate the dimeric $[Dy_2(LH_2)(LH)]^+$ motif (Figure 1 and Scheme 1). Note that, in the formation of 1, the ligand has exclusively utilized the enol form to generate the Dy_2O_2 core. The enolate oxygen atoms (O3 and O7) of the ligand bridge the two metal centers affording a quadrilateral

https://doi.org/10.1021/acs.inorgchem.1c00249
Inorg. Chem. 2021, 60, 8530−8545

four-membered Dy_2O_2 core as deduced from the bond distances, Dy1−O3 = 2.359 Å, Dy1−O7 = 2.557 Å, Dy2−O3 = 2.516 Å, and Dy2−O7 = 2.341 Å. (See Figure 2). The Dy•••Dy distance and the two Dy−O−Dy angles in the central Dy_2O_2 cores are found to be 4.131 Å and 115.80(7)°, and 114.87(7)°, respectively. Because of the bridging coordination of the enolate form of the ligand, we believe that the azide ligand is forced to function as a terminal ligand to one of the lanthanide centers. On the other lanthanide center, the ninth coordination is provided by a neutral methanol. Overall, the dinuclear assembly contains two types of nine-coordinated Dy^{III} centers: Dy1 (coordination environment, 3N, 6O) and Dy2 (coordination environment, 4N, 5O).

In order to ascertain if other mono anions such as chloride would similarly bind in a monodentate fashion, we performed the reaction using $DyCl_3{\cdot}6H_2O$ as the starting material but in the absence of the additional azide ligand. Under these conditions, however, we were not able to isolate any pure crystalline products.

As alluded above, **1** contains two different types of Dy^{III} centers. While both the Dy1 and Dy2 are nine-coordinated, they are nonequivalent, because they are surrounded by slightly different coordination environments. Dy1 is bound by the deprotonated arm of the diethanolamine of ligand $[LH]^{3-}$ with the ninth coordination provided by neutral methanol, while Dy2 is bound by the neutral diethanolamine arm of $[LH_2]^{2-}$ with the ninth coordination provided by the azide ligand. The ligand in this assembly binds in two ways: one as $[LH_2]^{2-}$ and the other as $[LH]^{3-}$. In the latter, one of the diethanolamine arm is deprotonated. The bond lengths found in the deprotoated arm ($-CH_2-CH_2-O$ (O8) are consistent with literature precedents.[11f] SHAPE analysis reveals that the coordination geometry around Dy1 and Dy2 (and other analogues) can be described as spherical capped square antiprism (see Figure 3, as well as Table S4 in the Supporting Information).[32]

The Dy−O bond lengths fall in a range (2.217−2.557 Å). The $Dy-O_{methanol}$ (2.492 Å) bond length is slightly longer than those observed previously[31,33] The deprotonated $Dy-O_{diethanolamine}$ (O8) (2.312 Å) bond length is slightly longer than that observed in the literature, but smaller than the bond length involving the neutral diethanolamine arm.[11f] All the Dy−N bond lengths fall in a very narrow range, 2.487−2.636 Å, consistent with values found in the literature.[31] The bond angles, Dy1−O3−Dy2 and Dy1−O7−Dy2 are 115.80° and 117.86°, respectively (Figure 2 and Table 2).

The crystal structure of **1** reveals the presence of intramolecular and intermolecular hydrogen bonds leading to the formation of a 1D polymeric chain (see Figures S7 and S8 in the Supporting Information).

Magnetic Studies. *Static Magnetic Properties.* dc magnetic properties of the two complexes **1** and **2** were determined by measuring the thermal dependence of the molar magnetic susceptibility (χ_M) from 2 K to 300 K (Figure 4). The room-temperature values of the $\chi_M T$ product are 27.90 cm^3 K mol^{-1} and 22.42 cm^3 K mol^{-1}, close to the expected values of 28.34 cm^3 K mol^{-1} and 23.64 cm^3 K mol^{-1}, respectively, for two isolated Dy^{III} ions ($^6H_{15/2}$ and $g_J = 4/3$) and Tb^{III} ($^7F_6$ and $g_J = 3/2$).[34] On cooling, $\chi_M T$ of **1** monotonously decreases down to 25 K, temperature for which a plateau is almost observed, and then decreases progressively reaching a minimum of 23.60 cm^3 K mol^{-1} at 2 K. The $\chi_M T$ of **2** remains almost constant down to 75 K, then decreases to

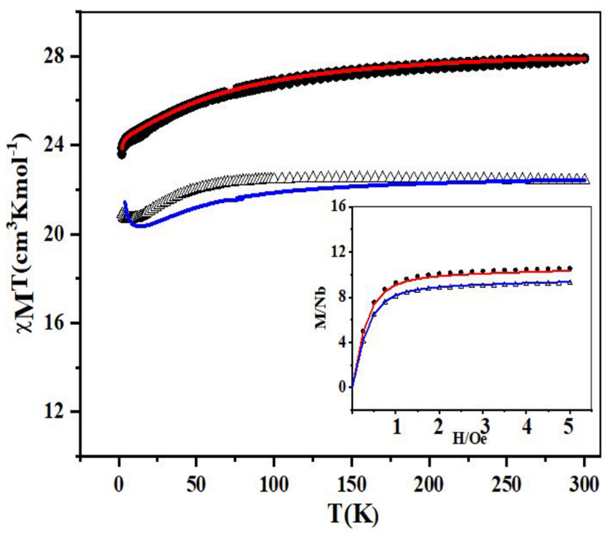

Figure 4. Thermal dependence of the $\chi_M T$ product for (●) **1** and (△) **2**. Red and blue lines correspond to the best simulated curves from POLY_ANISO program implemented in MOLCAS 8.2 package for complex **1** and **2**. *M* vs *H* plot at 2 K is fitted and given in the inset.

reach the value of 20.68 cm^3 K mol^{-1} at 8 K and finally slightly increases at very low temperature (20.88 cm^3 K mol^{-1} at 2 K). For both compounds **1** and **2**, the decrease can be mainly attributed to the depopulation of the ligand-field levels, while the change of slope at a lower temperature than 25 K could be due to the existence of weak magnetic interactions.

The field dependence of the magnetization has been measured for different temperatures from 2 K to 5 K. At 2 K, these show a classic behavior with values of 10.54 Nβ and 9.26 Nβ, respectively, for two Dy^{III} ions with the presence of a magnetically anisotropic ground state and two Tb^{III} ions (inset of Figure 4). Furthermore, the absence of a superposition in the different *M* vs *H* curves for each system (Figure S9 in the Supporting Information), elucidates the presence of significant magnetic anisotropy for **1** and **2**, as well as the possibility of low-lying excites states in the systems.

Dynamic Magnetic Properties. ac measurements have been performed for **1** and **2**. At zero dc magnetic field **1** displays a frequency dependence of the magnetic susceptibility in the temperature range of 2−15 K in the window 1−1000 Hz frequency of the oscillating field (see Figure 5a, as well as Figure S10 in the Supporting Information). The relaxation time (τ) has been extracted with an extended Debye model[35] (see Figure S11 and Table S6 in the Supporting Information). The Argand plot confirms that the observed slow magnetic relaxation corresponds to the entire sample (Figure S12 in the Supporting Information). The corresponding thermal variation of the log(τ) is depicted in Figure 5d and clearly shows a linear dependence (Orbach process) in the temperature range of 7−11 K, while a deviation from the linearity is observed down to 6 K, because of the presence of under-barrier processes such as Raman and quantum tunnelling of the magnetization (QTM). It is well-known that the latter can be canceled by applying a dc magnetic field.[36a,b] Thus, the field dependence of the magnetic susceptibility at 2 K (Figure S13 in the Supporting Information) shows an optimal behavior at a selected dc magnetic field value of 800 Oe (Figure 5b, as well as Table S7 in the Supporting Information). At 2 K and zero applied dc field, χ_M'' vs ν curve passes through a maximum at 5 Hz, which

https://doi.org/10.1021/acs.inorgchem.1c00249
Inorg. Chem. 2021, 60, 8530−8545

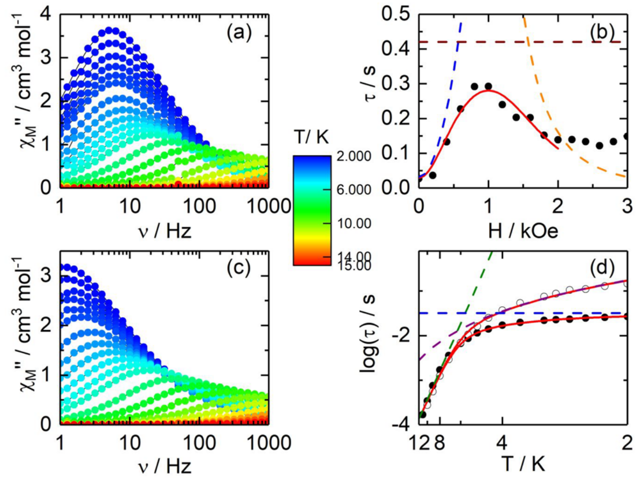

Figure 5. (a) Out-of-phase component of the ac magnetic susceptibility data for **1** in zero field in the temperature range of 2−15 K. (b) Field dependence of the magnetic relaxation time at 2 K in the field range of 0−3000 Oe with the full red line is the best-fitted curves (see text), while the dashed lines are the Orbach/Raman (brown), QTM (blue), and Direct (orange) contributions. (c) Out-of-phase component of the ac magnetic susceptibility data for **1** in 800 Oe in the temperature range of 2−15 K. (d) Thermal dependence of the magnetic relaxation time for **1** at (●) zero field in the 2−11 K temperature range and (○) 800 Oe applied magnetic field in the 2−10 K temperature range. Full lines are the best-fitted curves (see text) while the dashed lines are the Orbach (green), Raman (purple), and QTM (blue) contributions.

is shifted to 1 Hz upon applying a 800 Oe magnetic field (Figure 5c, as well as Figure S14 in the Supporting Information), because of the removal of the QTM contribution.

The relaxation time (τ) has been extracted with the extended Debye model (Table S7 in the Supporting Information) and the corresponding relaxation time of the magnetization in the temperature range of 2−11 K are given in Figure 5d, corresponding again to a general behavior of the sample as seen in the Argand plot (Figure S15 in the Supporting Information). As for **1** in zero field, the linear region depicted in the temperature dependence of the magnetic relaxation time has deviated at the lower temperatures, which is a sign of a remaining contribution of under energy barrier processes. At the optimal field of 800 Oe, the involvement of a significant Direct process or remaining QTM can be discarded. To support this affirmation, the τ vs H curve was fitted with the eq 1 for the 0−2000 Oe field range (Figure 6b).[36c,d]

$$\tau^{-1} = \frac{B_1}{1 + B_2H^2} + 2B_3H^m + B_4 \quad (1)$$

where the three terms correspond respectively to the QTM, Direct, and field-independent magnetic relaxation processes (Raman and Orbach). The best fit was obtained for B_1 = 31.25 s^{-1}; B_2 = 3.795(10) × 10^{-5} Oe^{-2}; B_3 = 1.95(4) × 10^{-13} s^{-1} K^{-1} Oe^{-4}; and B_4 = 2.38(4) s^{-1} leading to τ^{-1} (QTM) = 1.23 s^{-1} (blue contribution on Figure 5b), τ^{-1} (Direct) = 0.16 s^{-1} (orange contribution on Figure 5b) and τ^{-1} (Raman + Orbach) = 2.38 s^{-1} (brown contribution on Figure 5b). Thus, the thermal variation of the magnetic relaxation times could be fitted using a combination of Orbach and Raman processes.

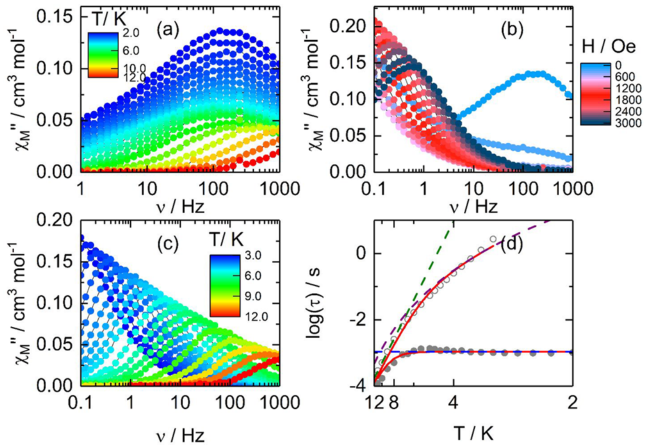

Figure 6. (a) Out-of-phase component of the ac magnetic susceptibility data for $\mathbf{1_{5\%}}$ in zero field in the temperature range of 2−15 K. (b) Out-of-phase component of the ac magnetic susceptibility data for $\mathbf{1_{5\%}}$ at 2 K from 0 to 3000 Oe. (c) Out-of-phase component of the ac magnetic susceptibility data for **1** in 800 Oe in the temperature range of 2−15 K. (d) Thermal dependence of the magnetic relaxation time for **1** in (●) zero field in the 2−11 K temperature range and (○) 800 Oe applied magnetic field in the 2−10 K temperature range. Full lines are the best-fitted curves (see text), while the dashed lines represent the Orbach (green), Raman (purple), and QTM (blue) contributions.

Since these two processes are field-independent (eq 2), they can be considered constant for both relaxation times at 0 and

$$\tau^{-1} = \underbrace{CT^n}_{\text{Raman}} + \underbrace{\tau_0^{-1}\exp\left(-\frac{\Delta}{kT}\right)}_{\text{Orbach}} + \underbrace{\tau_{\text{TI}}^{-1}}_{\text{QTM}}$$

800 Oe. Indeed, the thermal variation of the relaxation time is simultaneously fitted for **1** in zero field and 800 Oe with Orbach (Δ and τ_0) and Raman (C and n) shared parameters while QTM (τ_{TI}) appears only at 0 Oe. The best-fitted curves are represented in Figure 5d with Δ = 59(3) K, τ_0 = 10(4) × 10^{-6} s, C = 1.2(2) K^{-n} s^{-1}, n = 2.3(1) and τ_{TI} = 0.032(2) s. Importantly, τ_{TI} fitted from thermal variation matches the zero field limit of eq 1 (B_1^{-1}) obtained from field variations. The expected n value for Kramers ions should be 9,[37] but it is well-known that, for molecular systems,[38] the presence of both acoustic and optical phonons could lead to lower values, between 2 and 7.[39] A search in the literature reveals that Dy-based dimers show a most common coordination number of 8,[8,10] and more recently the tendency tries to go to low coordination systems.[8h] However, very few unsymmetric Dy-based dimers have been reported.[8a,10d,e,40a,g] The properties found in such complexes are consistent with the results found in this work. These results are summarized in Table 3.[8a,10d,e,40a,g] If one considers a similar coordination geometry, viz., the spherical capped square antiprism geometry, examples with field-induced relaxation are known.[41] In the present instance, however, we have observed zero-field SMM behavior.

The molecular structure of **1** highlighted two Dy^{III} ions in different coordination sphere, i.e., N3O6 and N4O5, respectively, for the Dy1 and Dy2 surroundings. One could expect two distinct magnetic behaviors while it was observed that both Dy^{III} centers are involved in the magnetic relaxation at the same frequency for a given temperature. The previous

https://doi.org/10.1021/acs.inorgchem.1c00249
Inorg. Chem. 2021, 60, 8530−8545

Table 3. Some Representative Examples of Dinuclear Dysprosium Complexes with Unsymmertrical Coordination Environment

compound	local geometries around Ln^{III} centers	magnetic properties	ref
$[Dy_2ovph_2Cl_2(MeOH)_3]$3 MeCN, H_2ovph = pyridine-2-carboxylic acid [(2-hydroxy-3-methoxyphenyl)methylene] hydrazide)	hula hoop-like geometry (center 1) and pentagonal bypyramidal (center 2)	SMM U_{eff} = 150 K, $\tau_0 = 2.3 \times 10^{-10}$ s U_{eff} = 198 K, $\tau_0 = 7.3 \times 10^{-9}$ s	8a
[hqH2]$[Dy_2(hq)_4(NO_3)_3]$ MeOH 8-hydroxyquinoline (hqH)	bicapped trigonal prism geometry	field-induced SMM U_{eff} = 41 cm $^{-1}$, $\tau_0 = 1.4 \times 10^{-6}$ s	10d
[(μ-mbpymNO)-{(tmh)3Dy}2] (tmh = 2,2,6,6-tetramethyl-3,5-heptanedionate mbpymNO = bipyrimidine-N-oxide	triangular dodecahedron and square-antiprismatic	SMM U_{eff} = 54.7 K, $\tau_0 = 1.7(3) \times 10^{-9}$; and U_{eff} = 47.8 K, $\tau_0 = 1.5(4) \times 10^{-9}$ s	10e
$[[Dy(Cy_3PO)_2$- (μ -Br)$(Br)_2]_2$ $2C_7H_8$(Cy_3PO = tricyclohexylphosphine oxide))	distorted octahedral	SMM U_{eff} = 684.1 K, $\tau_0 = 3.84 \times 10^{-12}$ s	40a
$[[Dy(Cy_3PO)_2$-(μ -I)$(I)_2]_2$ $4C_7H_8$(Cy_3PO = tricyclohexylphosphine oxide))	distorted octahedral	SMM U_{eff} = 1290 K, $\tau_0 = 1.26 \times 10^{-12}$ s	40b
$[Dy_2(Hhmb)_3(NCS)_3]$·2MeOH·py (H2hmb = *N*′-(2-hydroxy-3-methoxybenzylidene)- benzhydrazide)	monocapped distorted square antiprismatic geometry	field-induced SMM U_{eff} = 2.4 K, τ_0 = 0.16 s	40c
$[Dy_2(L1)_2(acac)_2(H_2O)]\cdot 2CH_2Cl_2$ L_1 = *N,N*-bis(salicylidene)-*o*-phenylenediamine	distorted square antiprism and capped trigonal prism	SMM U_{eff} = 36 K, $\tau_0 = 4.2 \times 10^{-7}$ s U_{eff} = 80 K, $\tau_0 = 8.3 \times 10^{-8}$ s	40d
[$Dy_2(L1)_2(DBM)_2(H_2O)]\cdot 2CH_2Cl_2$ L_1 = *N,N*-bis(salicylidene)-*o*-phenylenediamine, DBM = dibenzoylmethane	distorted square antiprism and capped trigonal prism	SMM U_{eff} = 31.4 K, $\tau_0 = 6.6 \times 10^{-7}$ s U_{eff} = 59.6 K, $\tau_0 = 7.3 \times 10^{-8}$ s	40e
$[Dy_2L_2(HL)(NO_3)(EtOH)]\cdot 0.5C_2H_5OH$ (LH_2 = 5-chloro-2-(((2-hydroxy-3-methoxybenzyl)imino)methyl) phenol)	triangular dodecahedron and square antiprism	SMM U_{eff} = 69.19 K, $\tau_0 = 9.5 \times 10^{-6}$ s U_{eff} = 45.73 K, $\tau_0 = 4.6 \times 10^{-6}$ s	40f
$(HNEt_3)[Dy_2(MQ)_4(NO_3)_3]\cdot EtOH\cdot H_2O$ (HMQ = 2-methyl-8-hydroxyquinoline)	square antiprism and spherical tricapped trigonal prism	slow relaxation of magnetization	40g
$[Dy_2(LH_2)(LH)(CH_3OH)(N_3)]\cdot 2H_2O$	capped square antiprismatic geometry	SMM U_{eff} = 59(3) K, $\tau_0 = 10(4) \times 10^{-6}$ s	this work

published dissymmetrical Dy^{III} dinuclear SMMs displayed either single[40a,b] or multiple[40d,g] relaxation contributions.

The magnetic properties of the diluted $\mathbf{1}_{5\%}$ analogue were studied in order to obtain a greater information on the slow relaxation mechanism in such Dy_2 SMM, especially to understand the effects of magnetic interactions within the dynamic magnetic properties in the dimer. The field dependence of the magnetization at 2 K (Figure S16 in the Supporting Information) shows a classic behavior with a value of 0.614 Nβ at 5 T, confirming a magnetic dilution of ~6%. $\mathbf{1}_{5\%}$ display an SMM behavior at zero applied field (see Figure 6, as well as Figures S17 and S18 in the Supporting Information), which is shifted to the higher frequencies (158 Hz), compared to **1** (5 Hz) at 2 K. Such shift is in agreement with a faster magnetic relaxation time when the magnetic interactions are canceled by magnetic dilution.

As previously, the extended Debye model was used in order to extract the temperature dependence of the relaxation mechanism (see Tables S8 and S9 in the Supporting Information), corresponding to a general behavior of the sample (Argand in Figure S15). Again, the thermal variation of the relaxation time is simultaneously fitted for zero field and 800 Oe field with Orbach parameters (Δ and τ_0), injected from the linear fit at high temperature region (from 8 K to 12 K) of the in-field relaxation curve (Figure 6d), and Raman (C and n) shared parameters, while QTM (τ_{TI}) appears only at 0 Oe. The best fitted curves are represented on Figure 6d with Δ = 66(1) K, $\tau_0 = 7.3(8) \times 10^{-7}$ s, $C = 9(3) \times 10^{-4}$ K^{-n} s^{-1}, n = 5.9(2), and $\tau_{TI} = 1.10(6) \times 10^{-3}$ s.

Figure 7 depicts the four thermal dependence of the relaxation times for **1** and $\mathbf{1}_{5\%}$. Indeed, at zero applied field, the suppression of the magnetic interactions between magnetic centers by magnetic dilution leads to an increase of the fast relaxation QTM process. However, under an applied magnetic field, the magnetization of the diluted sample relaxed slower than the magnetization of **1** (Figure 7) because of the decrease of the Raman contribution (T < 6 K) for $\mathbf{1}_{5\%}$, compared to **1**. Such diminution of the Raman contribution might be attributed to the diamagnetic dilution which reduces the interactions with the matrix. Such trend in the magnetic

https://doi.org/10.1021/acs.inorgchem.1c00249
Inorg. Chem. 2021, 60, 8530−8545

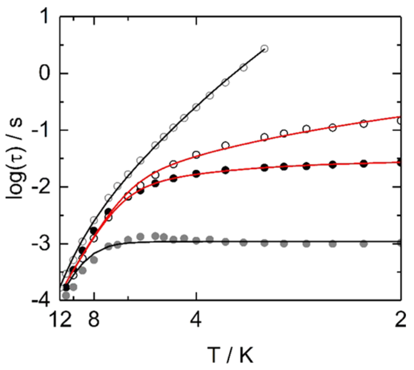

Figure 7. Thermal variation of the relaxation time for **1** at H = 0 Oe (full black spots) and H = 800 Oe (open black circles) and $\mathbf{1}_{5\%}$ at H = 0 Oe (full gray spots) and H = 800 Oe (open gray circles). Full red and black lines are the best-fitted curves (see text) for **1** and $\mathbf{1}_{5\%}$, respectively.

relaxation time can be reinforced by the behavior of the hysteresis loop of the magnetization of both compounds at 2 K. In which, once an applied magnetic field and the QTM is released, the hysteresis loop for $\mathbf{1}_{5\%}$ opens, in opposition to **1**, which remains closed (see Figure S21 in the Supporting Information).

At zero applied magnetic field, **2** was not displaying any out-of-phase component of the susceptibility at 2 K in the frequency window of the oscillating field (Figure S22 in the Supporting Information) (1−1000 Hz). Indeed, **2** involves non-Kramers Tb^{III} ions, which require a highly axial symmetric ligand field to possess a bistable ground state and prevent efficient QTM.[42] In order to cancel the possible QTM, the magnetic susceptibility has been measured under various applied magnetic field (Figure S23 in the Supporting Information). As soon as a dc field is applied, an out-of-phase contribution appears at 30 Hz which grows with the increase of the applied magnetic field. The 2800 Oe value is selected as the optimal applied magnetic field. At such field, the magnetic susceptibility displays a frequency dependence between 2 and 6 K (Figure S23), which is an indication of the slow magnetic relaxation for **2**. The thermal dependence of the relaxation time has been plotted by selecting, by hand, the maxima of the out-of-phase signal at each temperature (see Figure S24 in the Supporting Information). Considering the weak thermal dependence of the relaxation time and the 2800 Oe applied magnetic field value, one might suggest that the most probable magnetic relaxation occurs via a direct process ($\tau^{-1} = AH^4T$).

***Ab Initio* Calculations.** To investigate and quantify the nature of magnetic relaxations occurring at the individual magnetic center and for the entire complex, detailed multireference *ab initio* calculation has been performed for complexes **1** and **2**. The methodology employed here for the calculation is given in computational details (see the Experimental Section). First, the magnetic properties at the individual magnetic center have been calculated using the X-ray structures, wherein one of the Tb/Dy centers were replaced by a diamagnetic Lu^{III} ion. The calculations were performed on the entire complexes without further modeling.

Mechanism of Magnetic Relaxation by Individual Dy^{III}/Tb^{III} ions. Single ion calculations at the individual Ln^{III} center shows that the lowest-lying eight Kramer Doublets (KDs) behave differently for both centers, depending on the nature of the terminal coordination environment. For complex **1**, the low lying 8 KDs are lying in the range of 176.3−820.8 cm^{-1} for the Dy1 center, where methanol is coordinated, whereas for the Dy2 center, the ground to highest excited state lays in the range of 117.6−536.0 cm^{-1} (Table S12 in the Supporting Information), where terminal azide coordination is present. Although the splitting of 8 KDs is up to the range of 820.8 and 536.0 cm^{-1}, the relaxation is occurring at the first excited state, because of the displacement of the anisotropic axis at the excited state, compared to the ground state. The large difference for the two Dy centers is due to the difference in the crystal field effect provided by the two different terminal ligands and their influence on the geometry.[43] The MeOH terminal coordination provides stronger axial CF, compared to azide coordination. The required crystal field Hamiltonian is described as $H_{CF} = \sum_{k,q} B_k^q O_k^q$, where B_k^q is the crystal-field parameter and O_k^q is Steven's operator (Table S14 in the Supporting Information).[44] The axial parameter B_k^q (where k = 0 and q = 2) is comparatively larger for the Dy1 ion (−8.98), compared to the Dy2 site (−2.35). This is in agreement with our computed low lying energy splitting for the lowest eight doublets. To further understand the difference between electronic effects induced by the MeOH versus azide and geometric effects caused by the same, we performed additional calculations on model systems **1a** and **1b**. Here, model **1a** represents a structure where both Dy1 and Dy2 are coordinated to the methanol while model **1b** represents a structure where both the Dy^{III} centers are coordinated to an azide group. The energy splitting obtained for both the models **1a** (for **1a**-Dy1, 185.4−829.8 cm^{-1}; for **1a**-Dy2, 137.5−630.9 cm^{-1}) and **1b** (for **1b**-Dy1, 178.5−823.5 cm^{-1}; for **1b**-Dy2, 131.5 to 675 cm^{-1}) are similar to the original structures (see Table S12). This unequivocally reveals that the geometric effects due to the substitution play a prominent role in dictating the anisotropy and not the individual MeOH versus azide electronic effects. The analysis of Loprop charges also arrives at the same conclusion. Since the differences lie in the geometry, we looked at the SHAPE analysis, and this reveals that Dy1 has a CShM value of 1.432, while Dy2 has a value of 0.905, with respect to ideal nine-coordinated Muffine (MFF-9) geometry. Thus, stronger deviation from MFF-9 in Dy1 yields larger anisotropy, compared to Dy2.

Furthermore, to understand the magnetic relaxation contributed by the single Dy^{III} center, we have looked into the nature of the ground state for both the Dy^{III} centers. The ground state for Dy1 is of pure $m_J = \pm 15/2$ in nature, whereas for Dy2, a strong mixing of $m_J = \pm 15/2$ with other excited states is noticed. The U_{cal} values obtained for both the centers is 176.3 and 117.6 cm^{-1} respectively. The calculated energy barrier for magnetic relaxations is overestimated, compared to the experimental U_{eff} value. This suggests that the exchange interaction present between the $Dy^{III}\cdots Dy^{III}$ center/other under-barrier process/QTM effects alters the barrier height for magnetization reversal; hence, we looked at the exchange-coupled state of {Dy2} dimer. Although the nature of anisotropy at the ground level is *Ising* in nature (Table 4) for both Dy1 and Dy2 centers, the angle of deviation of the ground state axis (Figure 8) significantly deviates at the first excited state for Dy2 (∼7° vs ∼49°). The combination angle of deviation of the anisotropic axis and the contribution of higher excited state wave functions lead to different magnetic relaxations offered by Dy2.

https://doi.org/10.1021/acs.inorgchem.1c00249
Inorg. Chem. 2021, 60, 8530−8545

Table 4. *Ab Initio* Estimated *g*-Values, along with the Ground State Wave Function Estimated for 1 and Their Respective Models

complex	g_x	g_y	g_z	wave function contributions to the ground state
1-Dy1	0.0106	0.0171	19.9194	0.99| ± 15/2⟩
1-Dy2	0.0124	0.0199	19.7092	0.70| ± 15/2⟩ + 0.02| ± 13/2⟩ + 0.20| ± 11/2⟩ + 0.04| ± 9/2⟩
1a-Dy1	0.0083	0.0132	19.9226	0.99| ± 15/2⟩
1a-Dy2	0.0176	0.0280	19.7353	0.96| ± 15/2⟩⟩ + 0.03| ± 11/2⟩
1b-Dy1	0.0097	0.0162	19.9138	0.99| ± 15/2⟩
1b-Dy2	0.0271	0.0476	19.7406	0.96| ± 15/2⟩⟩ + 0.03| ± 11/2⟩

For complex **2**, the energy spectrum for the lowest *Ising* doublets is in the range of 0.3−535.5 cm^{-1} and 0.4−408.6 cm^{-1}, respectively, for Tb1 and Tb2 centers. Despite having significant ground-state anisotropy, the non-Kramer nature of the Tb^{III} ion leads to a significant tunnel splitting and lack of zero field SMM behavior for complex **2**. The tunnel splitting was found to be 0.19 and 0.15 cm^{-1} for Tb1 and Tb2 centers, respectively, as a result of different crystal field effects (see Table S13 in the Supporting Information). The ground-state anisotropic axis was plotted for both complexes **1** and **2** in Figure 9. The anisotropic axis for complex **1** lies parallel to each other in the same plane, which agrees well with the earlier reported Dy2 SMMs.[8a,h] In contrast, for complex **2**, a significant tilt between the g_{zz}-axis is noticed.

Mechanism of Magnetic Relaxation of Exchange Coupled State of 1 and 2. For the dinuclear-exchanged coupled state, the magnetic relaxation dynamics diagram for complex **1** is plotted in Figure 10, using POLY_ANISO calculations.[45] For complexes **1** and **2**, both the dipolar and exchange interactions were taken into account by using the Lines model, with the Hamiltonian given in eq 3 below.[46]

The Hamiltonian below is used to calculate the dipolar and exchange interaction between the $Ln^{III}\cdots Ln^{III}$ centers.

$$\hat{H}_{ex} = -\sum_i J_i S_i S_{i+1} \quad (3)$$

Here, $J_i = J_{idip} + J_{iexch}$; that is, J_i are the total magnetic interaction $Ln^{III}\cdots Ln^{III}$, this describes the interaction between the neighboring metal centers.

$$\hat{H} = -(-J_{dip}^{Ln^i-Ln^{i+1}} + J_{exch}^{Ln^i-Ln^{i+1}})\tilde{s}_{Ln_i}\tilde{s}_{Ln_{i+1}} \quad (4)$$

$$J_{dip}^{Ln^i-Ln^{i+1}} = \left(\frac{\mu_B{}^2}{R^3_{Dy^i-Dy^{i+1}}}\right) g^2_{Ln} \quad (5)$$

Lines model yields an excellent fit with the experimental data, and the extracted *J* values are given in Table 5. Note that the exchange interaction between $Dy^{III}\cdots Dy^{III}$ is weakly antiferromagnetic in nature, whereas for complex **2**, the interaction between $Tb^{III}\cdots Tb^{III}$ is found to ferromagnetic in nature. The mechanism of magnetization relaxation developed for the dinuclear model is shown in Figure 10. The mechanism computing using the POLY_ANISO routine yields a U_{cal} value of 69 cm^{-1} and this matches closely with experimental U_{eff} value (41 cm^{-1}). It has been observed that there is a discrepancy in the U_{eff} value obtained by experiment and U_{cal} value obtained from *ab initio* calculation for the exchange coupled state. Recently, we have reported an alternate equation to estimate the U_{cal} values for dinuclear Dy^{III} systems.[47] The equation is given as follows.

$$U_{cal\,eff} = \left[\frac{U_{cal1}}{(\text{QTM or TA-QTM}) \times 10^3} + \frac{U_{cal2}}{(\text{QTM or TA-QTM}) \times 10^3}\right] + 15J \quad (6)$$

Here, U_{cal1} and U_{cal2} represent the calculated energy barrier for the Dy1 and Dy2 centers, respectively, QTM or TA-QTM represents the value of transition propbabilities between ground states or excited state (one level below where the relaxation is happening). These values are taken from Figure 8, as well as Table S12 in the Supporting Information. Using the above formula, the $U_{cal\,eff}$ is now estimated to be 59 cm^{-1} (compare to 41 cm^{-1} experimental value). This value is

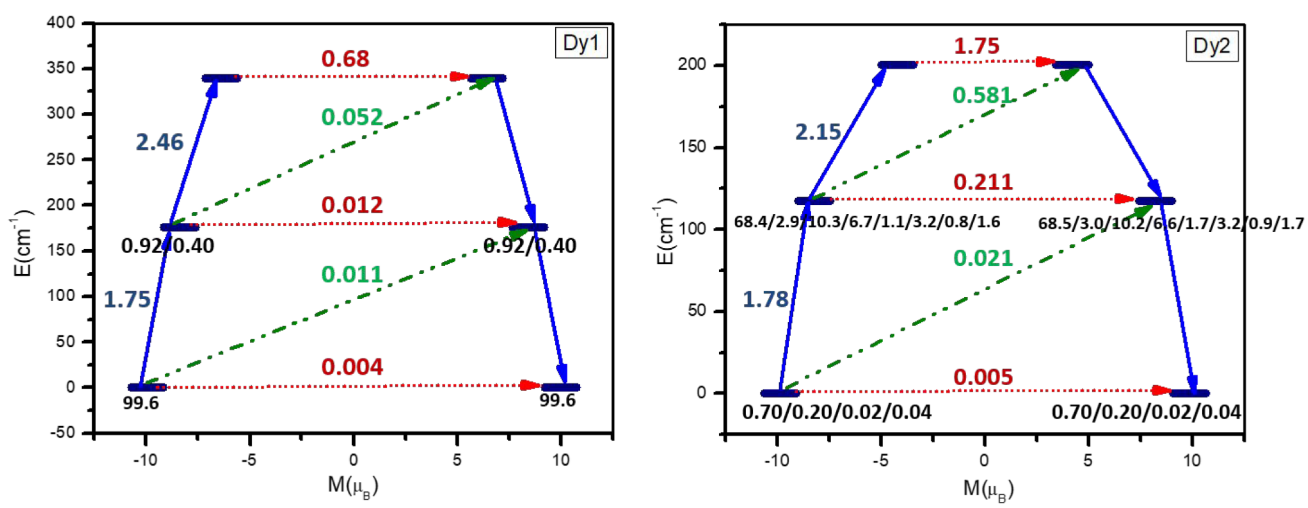

Figure 8. SINGLE_ANISO calculated relaxation pathways for Dy1 and Dy2 for complex **1**. The red line represents the QTM, blue line represents TA, and the green line represents the Orbach/Raman processes. The dark blue (smaller) line indicates the KDs as a function of magnetic moments. The number above these lines represents the transition probabilities from one m_J level to the other m_J level.

https://doi.org/10.1021/acs.inorgchem.1c00249
Inorg. Chem. 2021, 60, 8530−8545

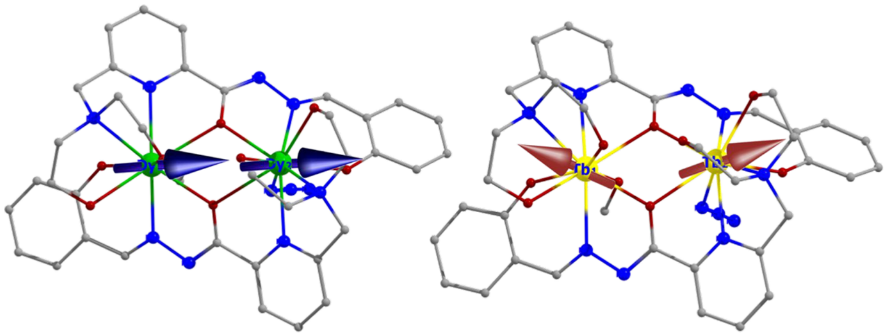

Figure 9. Arrangement of ground state anisotropy axes for complexes **1** and **2**.

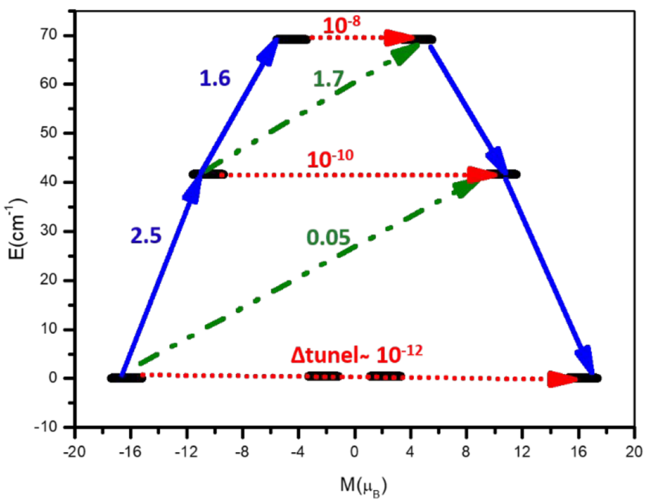

Figure 10. POLY_ANISO derived magnetic relaxation pathways for complex **1**. The red line represents the QTM, blue line represents TA, and green line represents the Orbach/Raman processes. The black line indicates the KDs as a function of magnetic moments. The number above these lines represents the transition probabilities from one m_J level to the other m_J level.

Table 5. *Ab Initio* and DFT Computed Exchange Values for Complex 1−3

	Ab Initio-Fitted (in cm^{-1})			DFT-Computed (cm^{-1})
complex	J_{ex}	J_{dip}	J_{tot}	J
1	−0.60	+0.15	−0.45	−0.55
2	+0.45	+0.13	+0.58	+0.60
3	–	–	–	+0.10

improved by 10 cm^{-1} though a small discrepancy is still there, in comparison to the experimental value.

The ferro-antiferro exchange obtained from complexes **1** and **2** is interesting and may be due to subtle structural factors, as argued below. Also note that the Lines model employed to extract these parameters is semiempirical and not fully *ab initio* as generally claimed. The alteration in the J values, however small, could be due to the very small structural distortions present inherently in complexes **1** and **2**, and we have earlier established that a small change in bond length or bond angle can lead to the switching of ferromagnetic to antiferromagnetic behavior.[30,47] Alternately, it could be purely dictated by the difference in anisotropy between **1** and **2**. To ascertain the origin further, DFT calculations were performed on the X-ray structure of **1** and **2** where the anisotropic ions are substituted by the isotropic Gd^{III} ions. These calculations clearly suggest the J value is antiferromagnetic in **1** and ferromagnetic in **2**. Since the sign is neatly reproduced in the DFT calculations, the nature of switch in the exchange clearly originates from small structural changes.

Furthermore, we have also performed DFT calculations on Gd^{III} analog of complexes **1** and **2** ($[Gd_2(LH_2)(LH)(CH_3OH)(N_3)]\cdot 2MeOH\cdot H_2O$ (**3**), see attached CIF files and Supplementary Information for further details) which yields a ferromagnetic J = +0.1 cm^{-1}. Furthermore, we have also performed DFT calculations on complex **3**, and this yields a ferromagnetic J = +0.1 cm^{-1}. The exchange values are verified with broken symmetry calculations performed by ORCA as well (+0.07 cm^{-1}). The spin density plots are given in Figure 11, and the spin density of 6.95 on Gd^{III} atom indicates spin delocalization. The mechanism of exchange coupling was studied in detail by us previously in {Gd2} dimer

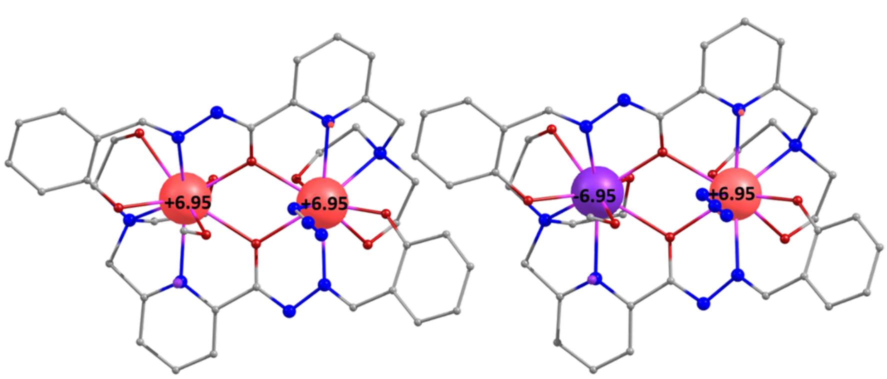

Figure 11. DFT computed spin density plot for complex **3**, the Gd^{III} analogue of complex **1** obtained from broken symmetry calculations; α and β densities are represented by red and violet lobes, respectively.

https://doi.org/10.1021/acs.inorgchem.1c00249
Inorg. Chem. 2021, 60, 8530−8545

bridged by μ-oxo bridges.[30] The nature of magnetic interactionis is strongly dependent on the Gd−O−Gd bond angles. A change of angle, even by 1°, can lead to a change in the nature of the coupling between the lanthanide ions. For complexes **2** and **3**, one of these angles between Tb−O−Tb and Gd−O−Gd are ∼114°, and for Dy−O−Dy it is 115°. These angles lie in the borderline area and may be responsible for the switch in the nature of exchange.

■ CONCLUSION

In summary, we have utilized a multidentate aroylhydrazone-based Schiff base ligand, 6-((bis(2-hydroxyethyl)amino)-*N*′-(2-hydroxybenzylidene)picolinohydrazide (LH_4) to assemble homometallic dinuclear lanthanide(III) complexes containing nonequivalent lanthanide metal centers $[Ln_2(LH_2)(LH)(CH_3OH)(N_3)]\cdot x\text{MeOH}\cdot yH_2O$ [**1**, Ln = Dy^{III}, x = 0, y = 2; **2**, Ln = Tb^{III}, x = 1, y = 1]. The nonequivalence of the lanthanide ions in these complexes arises from the variation of one terminal ligand. Thus, while one of the lanthanides has methanol as the ligand, the other has an azide. In all cases, the lanthanide ions are nine-coordinate in a spherical capped square antiprism geometry (as determined by SHAPE analysis). Detailed magnetic studies revealed that **1** is a zero-field SMM with an effective energy barrier (U_{eff}) 59(3) K of magnetization reversal and a relaxation time of τ_0 = 10(4) × 10^{-6} s, while **2** shows a field-induced SMM behavior. Combined *ab initio* and DFT calculations were performed to understand the observed magnetism. This reveals, that apart from the Kramers vs non-Kramers nature of the lanthanide ion, the individual variations in the coordination geometry around the lanthanide ions seem to play a subtle and important role in dictating the overall magnetic behavior. The change in the behavior of the nature of exchange has also been addressed in relation to the Ln−O−Ln bond angle which agrees with the earlier reported examples. The same magnetic structural correlation of the nature of exchange with metal oxo metal bond angle also holds true for the nine-coordinated asymmetric dinuclear lanthanide systems.

■ ASSOCIATED CONTENT

Supporting Information

The Supporting Information is available free of charge at https://pubs.acs.org/doi/10.1021/acs.inorgchem.1c00249.

Crystal data information for **3**, simulated single-crystal data and experimental XRD pattern for **1**−**2**, ESI-MS spectrum of complex **2** and **3**, molecular structure and bond length and bond angle of **2** and **3**, continuous shape measure calculations, supramolecular interactions. Field dependence of molar magnetization plot at 2 K and field dependence of molar magnetization plot in complexes and in-phase component of the ac magnetic susceptibility data for **1**, normalized Cole−Cole plot at several temperatures between 2 K and 15 K for **1** under 0 and 800 Oe, ac magnetic susceptibility data and normalized Cole−Cole plot at several temperatures between 2 K and 15 K for $\mathbf{1}_{5\%}$, in-phase and out-of-phase components of the ac magnetic susceptibility for **2** at 2 K in an applied DC magnetic field from 0 to 3000 Oe, in-phase (χ'_M) and out-of-phase (χ''_M) components of the ac magnetic susceptibility data for **2** in 2800 Oe applied magnetic field, CASSCF + RASSI-SO+SINGLE_ANISO computed energies of the eight low-lying KDs and SINGLE_ANISO computed crystal field parameters **1** and **2**, DFT computed spin density on Ln center using Broken symmetry approach for complexes **1**−**3** (PDF)

Accession Codes

CCDC 2026242, 2026261, 2026262, and 2058082 contain the supplementary crystallographic data for this paper. These data can be obtained free of charge via www.ccdc.cam.ac.uk/data_request/cif, or by emailing data_request@ccdc.cam.ac.uk, or by contacting The Cambridge Crystallographic Data Centre, 12 Union Road, Cambridge CB2 1EZ, UK; fax: +44 1223 336033.

■ AUTHOR INFORMATION

Corresponding Authors

Vadapalli Chandrasekhar − *Department of Chemistry, Indian Institute of Technology−Kanpur, Kanpur 208016, India; Tata Institute of Fundamental Research, Gopanpally, Hyderabad 500107, India;* orcid.org/0000-0003-1968-2980; Email: vc@iitk.ac.in, vc@tifrh.res.in

Fabrice Pointillart − *Université de Rennes, CNRS, ISCR (Institut des Sciences Chimiques de Rennes)-UMR 6226, F-35000 Rennes, France;* orcid.org/0000-0001-7601-1927; Email: fabrice.pointillart@univ-rennes1.fr

Gopalan Rajaraman − *Department of Chemistry, Indian Institute of Technology−Bombay, Powai 400076, Mumbai;* orcid.org/0000-0001-6133-3026; Email: rajaraman@chem.iitb.ac.in

Authors

Pawan Kumar − *Department of Chemistry, Indian Institute of Technology−Kanpur, Kanpur 208016, India*

Sourav Biswas − *Department of Geo-Chemistry, Keshav Deva Malaviya Institute of Petroleum Exploration, Dehradun 248915, India*

Abinash Swain − *Department of Chemistry, Indian Institute of Technology−Bombay, Powai 400076, Mumbai*

Joydev Acharya − *Department of Chemistry, Indian Institute of Technology−Kanpur, Kanpur 208016, India;* orcid.org/0000-0002-9480-4725

Vierandra Kumar − *Department of Chemistry, Indian Institute of Technology−Kanpur, Kanpur 208016, India*

Pankaj Kalita − *Tata Institute of Fundamental Research, Gopanpally, Hyderabad 500107, India;* orcid.org/0000-0002-1240-5633

Jessica Flores Gonzalez − *Université de Rennes, CNRS, ISCR (Institut des Sciences Chimiques de Rennes)-UMR 6226, F-35000 Rennes, France*

Olivier Cador − *Université de Rennes, CNRS, ISCR (Institut des Sciences Chimiques de Rennes)-UMR 6226, F-35000 Rennes, France;* orcid.org/0000-0003-2064-6223

Complete contact information is available at: https://pubs.acs.org/10.1021/acs.inorgchem.1c00249

Notes

The authors declare no competing financial interest.

■ ACKNOWLEDGMENTS

We thank the Department of Science and Technology (DST), India; the CNRS, Université de Rennes 1, the European Commission through the ERC-CoG 725184 MULTIPROSMM (Project No. 725184) for financial support, and also support for the Single Crystal CCD X-ray Diffractometer facility at IIT-Kanpur. V.C. is grateful to the DST for a J. C. Bose fellowship. P.K. and A.S. thank the University Grants Commission (UGC), India for Senior Research Fellowships. G.R. acknowledges DST/SERB for funding (Nos. CRG/2018/000430, DST/SJF/CSA-03/2018-10, SB/SJF/2019-20/12). We sincerely thank Mr. Prakash Nayak, NISER, Bhubanswar, Odisha, India, for the PXRD measurements.

■ REFERENCES

(1) (a) Sessoli, R.; Powell, A. K. Strategies towards single molecule magnets based on lanthanide ions. *Coord. Chem. Rev.* **2009**, *253*, 2328−2341. (b) Woodruff, D. N.; Winpenny, R. E. P.; Layfield, R. A. Lanthanide Single-Molecule Magnets. *Chem. Rev.* **2013**, *113*, 5110−5148. (c) Feltham, H. L. C.; Brooker, S. Review of purely 4f and mixed-metal and-4f single-molecule magnets containing only one lanthanide ion. *Coord. Chem. Rev.* **2014**, *276*, 1−33. (d) Liu, K.; Shi, W.; Cheng, P. Toward heterometallic single-molecule magnets: Synthetic strategy, structures and properties of 3d-4f discrete complexes. *Coord. Chem. Rev.* **2015**, *289−290*, 74−122. (e) Bar, A. K.; Pichon, C.; Sutter, J.-P. Magnetic anisotropy in two- to eight-coordinated transition-metal complexes: Recent developments in molecular magnetism. *Coord. Chem. Rev.* **2016**, *308*, 346−380. (f) Feng, M.; Tong, M.-L. Single Ion Magnets from 3d to 5f: Developments and Strategies. *Chem. - Eur. J.* **2018**, *24*, 7574−7594.

(2) Sessoli, R.; Gatteschi, D.; Caneschi, A.; Novak, M. A. Magnetic bistability in a metal-ion cluster. *Nature* **1993**, *365*, 141−143.

(3) (a) Dey, A.; Kalita, P.; Chandrasekhar, V. Lanthanide(III)-Based Single-Ion Magnets. *ACS Omega* **2018**, *3*, 9462−9475. (b) Liu, J.-L.; Chen, Y.-C.; Tong, M.-L. Symmetry strategies for high performance lanthanide-based single-molecule magnets. *Chem. Soc. Rev.* **2018**, *47*, 2431−2453.

(4) Ishikawa, N.; Sugita, M.; Ishikawa, T.; Koshihara, S.-y.; Kaizu, Y. Lanthanide Double-Decker Complexes Functioning as Magnets at the Single-Molecular Level. *J. Am. Chem. Soc.* **2003**, *125*, 8694−8695.

(5) (a) Ding, Y.-S.; Chilton, N. F.; Winpenny, R. E. P.; Zheng, Y.-Z. On Approaching the Limit of Molecular Magnetic Anisotropy: A Near-Perfect Pentagonal Bipyramidal Dysprosium(III) Single-Molecule Magnet. *Angew. Chem., Int. Ed.* **2016**, *55*, 16071−16074. (b) Liu, J.; Chen, Y.-C.; Liu, J.-L.; Vieru, V.; Ungur, L.; Jia, J.-H.; Chibotaru, L. F.; Lan, Y.; Wernsdorfer, W.; Gao, S.; Chen, X.-M.; Tong, M.-L. A Stable Pentagonal Bipyramidal Dy(III) Single-Ion Magnet with a Record Magnetization Reversal Barrier over 1000 K. *J. Am. Chem. Soc.* **2016**, *138*, 5441−5450. (c) Guo, F.-S.; Day, B. M.; Chen, Y.-C.; Tong, M.-L.; Mansikkamäki, A.; Layfield, R. A. A Dysprosium Metallocene Single-Molecule Magnet Functioning at the Axial Limit. *Angew. Chem., Int. Ed.* **2017**, *56*, 11445−11449. (d) Jiang, Z.; Sun, L.; Yang, Q.; Yin, B.; Ke, H.; Han, J.; Wei, Q.; Xie, G.; Chen, S. Excess axial electrostatic repulsion as a criterion for pentagonal bipyramidal DyIII single-ion magnets with high Ueff and TB. *J. Mater. Chem. C* **2018**, *6*, 4273−4280.

(6) (a) Rinehart, J. D.; Fang, M.; Evans, W. J.; Long, J. R. A N23-Radical-Bridged Terbium Complex Exhibiting Magnetic Hysteresis at 14 K. *J. Am. Chem. Soc.* **2011**, *133*, 14236−14239. (b) Chen, Y.-C.; Liu, J.-L.; Ungur, L.; Liu, J.; Li, Q.-W.; Wang, L.-F.; Ni, Z.-P.; Chibotaru, L. F.; Chen, X.-M.; Tong, M.-L. Symmetry-Supported Magnetic Blocking at 20 K in Pentagonal Bipyramidal Dy(III) Single-Ion Magnets. *J. Am. Chem. Soc.* **2016**, *138*, 2829−2837. (c) Gupta, S. K.; Rajeshkumar, T.; Rajaraman, G.; Murugavel, R. An air-stable Dy(iii) single-ion magnet with high anisotropy barrier and blocking temperature. *Chem. Sci.* **2016**, *7*, 5181−5191. (d) Goodwin, C. A. P.; Ortu, F.; Reta, D.; Chilton, N. F.; Mills, D. P. Molecular magnetic hysteresis at 60 K in dysprosocenium. *Nature* **2017**, *548*, 439−442. (e) Guo, F.-S.; Day, B. M.; Chen, Y.-C.; Tong, M.-L.; Mansikkamäki, A.; Layfield, R. A. Magnetic hysteresis up to 80 K in a dysprosium metallocene single-molecule magnet. *Science* **2018**, *362*, 1400−1403. (f) Randall McClain, K.; Gould, C. A.; Chakarawet, K.; Teat, S. J.; Groshens, T. J.; Long, J. R.; Harvey, B. G. High-temperature magnetic blocking and magneto-structural correlations in a series of dysprosium(iii) metallocenium single-molecule magnets. *Chem. Sci.* **2018**, *9*, 8492−8503.

(7) Lu, J.; Guo, M.; Tang, J. Recent Developments in Lanthanide Single-Molecule Magnets. *Chem. - Asian J.* **2017**, *12*, 2772−2779.

(8) (a) Guo, Y.-N.; Xu, G.-F.; Wernsdorfer, W.; Ungur, L.; Guo, Y.; Tang, J.; Zhang, H.-J.; Chibotaru, L. F.; Powell, A. K. Strong Axiality and Ising Exchange Interaction Suppress Zero-Field Tunneling of Magnetization of an Asymmetric Dy2 Single-Molecule Magnet. *J. Am. Chem. Soc.* **2011**, *133*, 11948−11951. (b) Long, J.; Habib, F.; Lin, P.-H.; Korobkov, I.; Enright, G.; Ungur, L.; Wernsdorfer, W.; Chibotaru, L. F.; Murugesu, M. Single-Molecule Magnet Behavior for an Antiferromagnetically Superexchange-Coupled Dinuclear Dysprosium(III) Complex. *J. Am. Chem. Soc.* **2011**, *133*, 5319−5328. (c) Rinehart, J. D.; Fang, M.; Evans, W. J.; Long, J. R. Strong exchange and magnetic blocking in N23–radical-bridged lanthanide complexes. *Nat. Chem.* **2011**, *3*, 538−542. (d) Mazarakioti, E. C.; Regier, J.; Cunha-Silva, L.; Wernsdorfer, W.; Pilkington, M.; Tang, J.; Stamatatos, T. C. Large Energy Barrier and Magnetization Hysteresis at 5 K for a Symmetric {Dy2} Complex with Spherical Tricapped Trigonal Prismatic DyIII Ions. *Inorg. Chem.* **2017**, *56*, 3568−3578. (e) Zhang, L.; Zhang, Y.-Q.; Zhang, P.; Zhao, L.; Guo, M.; Tang, J. Single-Molecule Magnet Behavior Enhanced by Synergic Effect of Single-Ion Anisotropy and Magnetic Interactions. *Inorg. Chem.* **2017**, *56*, 7882−7889. (f) Guo, F.-S.; Layfield, R. A. Strong direct exchange coupling and single-molecule magnetism in indigo-bridged lanthanide dimers. *Chem. Commun.* **2017**, *53*, 3130−3133. (g) Guo, M.; Zhang, Y.-Q.; Zhu, Z.; Tang, J. Dysprosium Compounds with Hula-Hoop-like Geometries: The Influence of Magnetic Anisotropy and Magnetic Interactions on Magnetic Relaxation. *Inorg. Chem.* **2018**, *57*, 12213−12221. (h) Han, T.; Ding, Y.-S.; Li, Z.-H.; Yu, K.-X.; Zhai, Y.-Q.; Chilton, N. F.; Zheng, Y.-Z. A dichlorido-bridged dinuclear Dy(iii) single-molecule magnet with an effective energy barrier larger than 600 K. *Chem. Commun.* **2019**, *55*, 7930−7933. (i) Pointillart, F.; Le Gal, Y.; Golhen, S.; Cador, O.; Ouahab, L. Single-Molecule Magnet Behaviour in a Tetrathiafulvalene-Based Electroactive Antiferromagnetically Coupled Dinuclear Dysprosium(III) Complex. *Chem. - Eur. J.* **2011**, *17*, 10397−10404. (j) Chow, C. Y.; Bolvin, H.; Campbell, V. E.; Guillot, R.; Kampf, J. W.; Wernsdorfer, W.; Gendron, F.; Autschbach, J.; Pecoraro, V. L.; Mallah, T. Assessing the exchange coupling in binuclear lanthanide(iii) complexes and the slow relaxation of the magnetization in the antiferromagnetically coupled Dy2 derivative. *Chem. Sci.* **2015**, *6*, 4148−4159.

(9) Wernsdorfer, W.; Aliaga-Alcalde, N.; Hendrickson, D. N.; Christou, G. Exchange-biased quantum tunnelling in a supramolecular dimer of single-molecule magnets. *Nature* **2002**, *416*, 406−409.

(10) (a) Aguilà, D.; Barrios, L. A.; Velasco, V.; Arnedo, L.; Aliaga-Alcalde, N.; Menelaou, M.; Teat, S. J.; Roubeau, O.; Luis, F.; Aromí, G. Lanthanide Contraction within a Series of Asymmetric Dinuclear [Ln2] Complexes. *Chem. - Eur. J.* **2013**, *19*, 5881−5891. (b) Aguilà, D.; Barrios, L. A.; Velasco, V.; Roubeau, O.; Repollés, A.; Alonso, P. J.; Sesé, J.; Teat, S. J.; Luis, F.; Aromí, G. Heterodimetallic [LnLn′] Lanthanide Complexes: Toward a Chemical Design of Two-Qubit Molecular Spin Quantum Gates. *J. Am. Chem. Soc.* **2014**, *136*, 14215−14222. (c) González-Fabra, J.; Bandeira, N. A. G.; Velasco, V.; Barrios, L. A.; Aguilà, D.; Teat, S. J.; Roubeau, O.; Bo, C.; Aromí, G. Thermodynamic Stability of Heterodimetallic [LnLn′] Complexes: Synthesis and DFT Studies. *Chem. - Eur. J.* **2017**, *23*, 5117−5125. (d) Moreno Pineda, E.; Chilton, N. F.; Marx, R.; Dörfel, M.; Sells, D. O.; Neugebauer, P.; Jiang, S.-D.; Collison, D.; van Slageren, J.; McInnes, E. J. L.; Winpenny, R. E. P. Direct measurement of dysprosium(III)···dysprosium(III) interactions in a single-molecule magnet. *Nat. Commun.* **2014**, *5*, 5243−5249. (e) Díaz-Ortega, I. F.; Herrera, J. M.; Aravena, D.; Ruiz, E.; Gupta, T.; Rajaraman, G.; Nojiri, H.; Colacio, E. Designing a Dy2 Single-Molecule Magnet with Two Well-Differentiated Relaxation Processes by Using a Nonsymmetric Bis-bidentate Bipyrimidine-N-Oxide Ligand: A Comparison with Mononuclear Counterparts. *Inorg. Chem.* **2018**, *57*, 6362−6375.

(11) (a) Chandrasekhar, V.; Bag, P.; Colacio, E. Octanuclear {Ln(III)8}(Ln = Gd, Tb, Dy, Ho) Macrocyclic Complexes in a

Cyclooctadiene-like Conformation: Manifestation of Slow Relaxation of Magnetization in the Dy(III) Derivative. *Inorg. Chem.* **2013**, *52*, 4562−4570. (b) Das, S.; Dey, A.; Kundu, S.; Biswas, S.; Narayanan, R. S.; Titos-Padilla, S.; Lorusso, G.; Evangelisti, M.; Colacio, E.; Chandrasekhar, V. Decanuclear Ln10 Wheels and Vertex-Shared Spirocyclic Ln5 Cores: Synthesis, Structure, SMM Behavior, and MCE Properties. *Chem. - Eur. J.* **2015**, *21*, 16955−16967. (c) Das, S.; Hossain, S.; Dey, A.; Biswas, S.; Sutter, J.-P.; Chandrasekhar, V. Molecular Magnets Based on Homometallic Hexanuclear Lanthanide-(III) Complexes. *Inorg. Chem.* **2014**, *53*, 5020−5028. (d) Biswas, S.; Das, S.; Acharya, J.; Kumar, V.; van Leusen, J.; Kögerler, P.; Herrera, J. M.; Colacio, E.; Chandrasekhar, V. Homometallic DyIII Complexes of Varying Nuclearity from 2 to 21: Synthesis, Structure, and Magnetism. *Chem. - Eur. J.* **2017**, *23*, 5154−5170. (e) Biswas, S.; Bejoymohandas, K. S.; Das, S.; Kalita, P.; Reddy, M. L. P.; Oyarzabal, I.; Colacio, E.; Chandrasekhar, V. Mononuclear Lanthanide Complexes: Energy-Barrier Enhancement by Ligand Substitution in Field-Induced DyIII SIMs. *Inorg. Chem.* **2017**, *56*, 7985−7997. (f) Biswas, S.; Das, S.; Gupta, T.; Singh, S. K.; Pissas, M.; Rajaraman, G.; Chandrasekhar, V. Observation of Slow Relaxation and Single-Molecule Toroidal Behavior in a Family of Butterfly-Shaped Ln4 Complexes. *Chem. - Eur. J.* **2016**, *22*, 18532−18550. (g) Kalita, P.; Ahmed, N.; Bar, A. K.; Dey, S.; Jana, A.; Rajaraman, G.; Sutter, J.-P.; Chandrasekhar, V. Pentagonal Bipyramidal Ln(III) Complexes Containing an Axial Phosphine Oxide Ligand: Field-induced Single-ion Magnetism Behavior of the Dy(III) Analogues. *Inorg. Chem.* **2020**, *59*, 6603−6612.

(12) (a) Guo, Y.-N.; Xu, G.-F.; Gamez, P.; Zhao, L.; Lin, S.-Y.; Deng, R.; Tang, J.; Zhang, H.-J. Two-Step Relaxation in a Linear Tetranuclear Dysprosium(III) Aggregate Showing Single-Molecule Magnet Behavior. *J. Am. Chem. Soc.* **2010**, *132*, 8538−8539. (b) Guo, Y.-N.; Chen, X.-H.; Xue, S.; Tang, J. Modulating Magnetic Dynamics of Three Dy2 Complexes through Keto-Enol Tautomerism of the o-Vanillin Picolinoylhydrazone Ligand. *Inorg. Chem.* **2011**, *50*, 9705−9713. (c) Xue, S.; Guo, Y.-N.; Ungur, L.; Tang, J.; Chibotaru, L. F. Tuning the Magnetic Interactions and Relaxation Dynamics of Dy2 Single-Molecule Magnets. *Chem. - Eur. J.* **2015**, *21*, 14099−14106. (d) Ma, F.; Chen, Q.; Xiong, J.; Sun, H.-L.; Zhang, Y.-Q.; Gao, S. Modulating Slow Magnetic Relaxation of Dysprosium Compounds through the Position of Coordinating Nitrate Group. *Inorg. Chem.* **2017**, *56*, 13430−13436. (e) Bazhenova, T. A.; Mironov, V. S.; Yakushev, I. A.; Svetogorov, R. D.; Maximova, O. V.; Manakin, Y. V.; Kornev, A. B.; Vasiliev, A. N.; Yagubskii, E. B. End-to-End Azido-Bridged Lanthanide Chain Complexes (Dy, Er, Gd, and Y) with a Pentadentate Schiff-Base [N3O2] Ligand: Synthesis, Structure, and Magnetism. *Inorg. Chem.* **2020**, *59*, 563−578.

(13) (a) Hong, C. S.; Koo, J.-e.; Son, S.-K.; Lee, Y. S.; Kim, Y.-S.; Do, Y. Unusual Ferromagnetic Couplings in Single End-to-End Azide-Bridged Cobalt(II) and Nickel(II) Chain Systems. *Chem. - Eur. J.* **2001**, *7*, 4243−4252. (b) Escuer, A.; Esteban, J.; Perlepes, S. P.; Stamatatos, T. C. The bridging azido ligand as a central "player" in high-nuclearity 3d-metal cluster chemistry. *Coord. Chem. Rev.* **2014**, *275*, 87−129.

(14) (a) Vogel, A. I.; Furniss, B. S.; Hannaford, A. J.; Smith, P. W. G.; Tatchell, A. R. *Vogel's Textbook of Practical Organic Chemistry*, 5th Edition; Longman: Harlow, U.K., 1989. (b) Williams, D. B. G.; Lawton, M. Drying of Organic Solvents: Quantitative Evaluation of the Efficiency of Several Desiccants. *J. Org. Chem.* **2010**, *75*, 8351−8354.

(15) Zeng, X.; Coquière, D.; Alenda, A.; Garrier, E.; Prangé, T.; Li, Y.; Reinaud, O.; Jabin, I. Efficient Synthesis of Calix[6]tmpa: A New Calix[6]azacryptand with Unique Conformational and Host-Guest Properties. *Chem. - Eur. J.* **2006**, *12*, 6393−6402.

(16) *SMART SAINT, Software Reference Manuals*, Version 6.45; 2003.

(17) Sheldrick, G. *SADABS, Software for Empirical Absorption Correction*, Version 2.05; University of Göttingen: Göttingen, Germany, 2002.

(18) *SHELXTL Reference Manual*; Bruker Analytical X-ray Systems, Inc.: Madison, WI, 2000.

(19) CrysAlis PRO *Rigaku Oxford Diffraction*; Yarnton, England, 2015.

(20) Sheldrick, G. A short history of SHELX. *Acta Crystallogr., Sect. A: Found. Crystallogr.* **2008**, *64*, 112−122.

(21) Dolomanov, O. V.; Bourhis, L. J.; Gildea, R. J.; Howard, J. A. K.; Puschmann, H. OLEX2: a complete structure solution, refinement and analysis program. *J. Appl. Crystallogr.* **2009**, *42*, 339−341.

(22) Bradenburg, K. *Diamond*, Version 3.1 e; Crystal Impact GbR: Bonn, Germany, 2005.

(23) (a) Aquilante, F.; Autschbach, J.; Carlson, R. K.; Chibotaru, L. F.; Delcey, M. G.; De Vico, L.; Fdez Galván, I.; Ferré, N.; Frutos, L. M.; Gagliardi, L.; Garavelli, M.; Giussani, A.; Hoyer, C. E.; Li Manni, G.; Lischka, H.; Ma, D.; Malmqvist, P. Å.; Müller, T.; Nenov, A.; Olivucci, M.; Pedersen, T. B.; Peng, D.; Plasser, F.; Pritchard, B.; Reiher, M.; Rivalta, I.; Schapiro, I.; Segarra-Martí, J.; Stenrup, M.; Truhlar, D. G.; Ungur, L.; Valentini, A.; Vancoillie, S.; Veryazov, V.; Vysotskiy, V. P.; Weingart, O.; Zapata, F.; Lindh, R. Molcas 8: New capabilities for multiconfigurational quantum chemical calculations across the periodic table. *J. Comput. Chem.* **2016**, *37*, 506−541. (b) Duncan, J. A. MOLCAS 7.2. *J. Am. Chem. Soc.* **2009**, *131*, 2416−2416. (c) Veryazov, V.; Widmark, P.-O.; Serrano-Andrés, L.; Lindh, R.; Roos, B. O. 2MOLCAS as a development platform for quantum chemistry software. *Int. J. Quantum Chem.* **2004**, *100*, 626−635. (d) Aquilante, F.; De Vico, L.; Ferré, N.; Ghigo, G.; Malmqvist, P.-å.; Neogrády, P.; Pedersen, T. B.; Pitoňák, M.; Reiher, M.; Roos, B. O.; Serrano-Andrés, L.; Urban, M.; Veryazov, V.; Lindh, R. MOLCAS 7: The Next Generation. *J. Comput. Chem.* **2010**, *31*, 224−247.

(24) (a) Ungur, L.; Van den Heuvel, W.; Chibotaru, L. F. Ab initio investigation of the non-collinear magnetic structure and the lowest magnetic excitations in dysprosium triangles. *New J. Chem.* **2009**, *33*, 1224−1230. (b) Chibotaru, L. F.; Ungur, L.; Aronica, C.; Elmoll, H.; Pilet, G.; Luneau, D. Structure, Magnetism, and Theoretical Study of a Mixed-Valence CoII3CoIII4 Heptanuclear Wheel: Lack of SMM Behavior despite Negative Magnetic Anisotropy. *J. Am. Chem. Soc.* **2008**, *130*, 12445−12455. (c) Chibotaru, L. F.; Ungur, L.; Soncini, A. The Origin of Nonmagnetic Kramers Doublets in the Ground State of Dysprosium Triangles: Evidence for a Toroidal Magnetic Moment. *Angew. Chem., Int. Ed.* **2008**, *47*, 4126−4129.

(25) (a) Vignesh, K. R.; Langley, S. K.; Murray, K. S.; Rajaraman, G. Exploring the Influence of Diamagnetic Ions on the Mechanism of Magnetization Relaxation in {CoIII2LnIII2} (Ln = Dy, Tb, Ho) "Butterfly" Complexes. *Inorg. Chem.* **2017**, *56*, 2518−2532. (b) Chilton, N. F.; Anderson, R. P.; Turner, L. D.; Soncini, A.; Murray, K. S. PHI: A powerful new program for the analysis of anisotropic monomeric and exchange-coupled polynuclear d- and f-block complexes. *J. Comput. Chem.* **2013**, *34*, 1164−1175.

(26) (a) Singh, M. K.; Rajaraman, G. Acquiring a record barrier height for magnetization reversal in lanthanide encapsulated fullerene molecules using DFT and ab initio calculations. *Chem. Commun.* **2016**, *52*, 14047−14050. (b) Singh, M. K.; Yadav, N.; Rajaraman, G. Record high magnetic exchange and magnetization blockade in Ln2@C79N (Ln = Gd(iii) and Dy(iii)) molecules: a theoretical perspective. *Chem. Commun.* **2015**, *51*, 17732−17735. (c) Bar, A. K.; Kalita, P.; Singh, M. K.; Rajaraman, G.; Chandrasekhar, V. Low-coordinate mononuclear lanthanide complexes as molecular nanomagnets. *Coord. Chem. Rev.* **2018**, *367*, 163−216.

(27) Lines, M. E. Orbital Angular Momentum in the Theory of Paramagnetic Clusters. *J. Chem. Phys.* **1971**, *55*, 2977−2984.

(28) (a) Becke, A. D. Density-functional thermochemistry. III. The role of exact exchange. *J. Chem. Phys.* **1993**, *98*, 5648−5652. (b) Frisch, M.; Trucks, G.; Schlegel, H. B.; Scuseria, G. E.; Robb, M. A.; Cheeseman, J. R.; Scalmani, G.; Barone, V.; Mennucci, B.; Petersson, G., et al.*Gaussian 09*, Revision d.01; Gaussian, Inc.: Wallingford, CT, 2009; p 201.

(29) (a) Cundari, T. R.; Stevens, W. J. Effective core potential methods for the lanthanides. *J. Chem. Phys.* **1993**, *98*, 5555−5565. (b) Schäfer, A.; Huber, C.; Ahlrichs, R. Fully optimized contracted

Gaussian basis sets of triple zeta valence quality for atoms Li to Kr. *J. Chem. Phys.* **1994**, *100*, 5829−5835.

(30) Rajeshkumar, T.; Singh, S. K.; Rajaraman, G. A computational perspective on magnetic coupling, magneto-structural correlations and magneto-caloric effect of a ferromagnetically coupled {GdIII-GdIII} Pair. *Polyhedron* **2013**, *52*, 1299−1305.

(31) Biswas, S.; Kumar, P.; Swain, A.; Gupta, T.; Kalita, P.; Kundu, S.; Rajaraman, G.; Chandrasekhar, V. Phosphonate-assisted tetranuclear lanthanide assemblies: observation of the toroidic ground state in the TbIII analogue. *Dalton Trans.* **2019**, *48*, 6421−6434.

(32) (a) Cirera, J.; Ruiz, E.; Alvarez, S. Continuous Shape Measures as a Stereochemical Tool in Organometallic Chemistry. *Organometallics* **2005**, *24*, 1556−1562. (b) *SHAPE: Continuous Shape Measures Calculation 2.1; Electronic Structure Group*; Universitat de Barcelona: Spain, 2013.

(33) Zou, L.; Zhao, L.; Chen, P.; Guo, Y.-N.; Guo, Y.; Li, Y.-H.; Tang, J. Phenoxido and alkoxido-bridged dinuclear dysprosium complexes showing single-molecule magnet behaviour. *Dalton Trans.* **2012**, *41*, 2966−2971.

(34) Kahn, O. *Molecular Magnetism*; VCH Publishers: New York, 1993; p 393.

(35) (a) Dekker, C.; Arts, A. F. M.; de Wijn, H. W.; van Duyneveldt, A. J.; Mydosh, J. A. Activated dynamics in a two-dimensional Ising spin glass: Activated dynamics in a two-dimensional Ising spin glass: Rb2Cu1-xCoxF4. *Phys. Rev. B: Condens. Matter Mater. Phys.* **1989**, *40*, 11243−11251. (b) Cole, K. S.; Cole, R. H. Dispersion and Absorption in Dielectrics I. Alternating Current Characteristics. *J. Chem. Phys.* **1941**, *9*, 341−351.

(36) (a) Car, P.-E.; Perfetti, M.; Mannini, M.; Favre, A.; Caneschi, A.; Sessoli, R. Giant field dependence of the low temperature relaxation of the magnetization in a dysprosium(iii)-DOTA complex. *Chem. Commun.* **2011**, *47*, 3751−3753. (b) Pointillart, F.; Flores Gonzalez, J.; Montigaud, V.; Tesi, L.; Cherkasov, V.; Le Guennic, B.; Cador, O.; Ouahab, L.; Sessoli, R.; Kuropatov, V. Redox- and solvato-magnetic switching in a tetrathiafulvalene-based triad single-molecule magnet. *Inorg. Chem. Front.* **2020**, *7*, 2322−2334. (c) Lucaccini, E.; Sorace, L.; Perfetti, M.; Costes, J.-P.; Sessoli, R. Beyond the anisotropy barrier: slow relaxation of the magnetization in both easy-axis and easy-plane Ln(trensal) complexes. *Chem. Commun.* **2014**, *50*, 1648−1651. (d) Pedersen, K. S.; Dreiser, J.; Weihe, H.; Sibille, R.; Johannesen, H. V.; Sorensen, M. A.; Nielsen, B. E.; Sigrist, M.; Mutka, H.; Rols, S.; Bendix, J.; Piligkos, S. Design of Single-Molecule Magnets: Insufficiency of the Anisotropy Barrier as the Sole Criterion. *Inorg. Chem.* **2015**, *54*, 7600−7606.

(37) Abragam, A.; Bleaney, B. *Electron Paramagnetic Resonance of Transition Ions*; Oxford University Press: Oxford, 2012.

(38) Goodwin, C. A. P.; Reta, D.; Ortu, F.; Chilton, N. F.; Mills, D. P. Synthesis and Electronic Structures of Heavy Lanthanide Metallocenium Cations. *J. Am. Chem. Soc.* **2017**, *139*, 18714−18724.

(39) (a) Singh, A.; Shrivastava, K. N. Optical-acoustic two-phonon relaxation in spin systems. *Phys. Status Solidi B* **1979**, *95*, 273−277. (b) Shrivastava, K. N. Theory of Spin-Lattice Relaxation. *Phys. Status Solidi B* **1983**, *117*, 437−458.

(40) (a) Li, M.; Wu, H.; Xia, Z.; Montigaud, V.; Cador, O.; Le Guennic, B.; Ke, H.; Wang, W.; Xie, G.; Chen, S. Bromine-bridged Dy2 single-molecule magnet: magnetic anisotropy driven by cis/trans stereoisomers. *Chem. Commun.* **2019**, *55*, 14661−14664. (b) Wu, H.; Li, M.; Xia, Z.; Montigaud, V.; Cador, O.; Le Guennic, B.; Ke, H.; Wang, W.; Xie, G.; Chen, S.; Gao, S. High temperature quantum tunnelling of magnetization and thousand kelvin anisotropy barrier in a Dy2 single-molecule magnet. *Chem. Commun.* **2021**, *57*, 371−374. (c) Hutchings, A.-J.; Habib, F.; Holmberg, R. J.; Korobkov, I.; Murugesu, M. Structural Rearrangement Through Lanthanide Contraction in Dinuclear Complexes. *Inorg. Chem.* **2014**, *53*, 2102−2112. (d) Lin, P.-H.; Sun, W.-B.; Yu, M.-F.; Li, G.-M.; Yan, P.-F.; Murugesu, M. An unsymmetrical coordination environment leading to two slow relaxation modes in a Dy2 single-molecule magnet. *Chem. Commun.* **2011**, *47*, 10993−10995. (e) Zhang, W.-Y.; Chen, P.; Tian, Y.-M.; Li, H.-F.; Sun, W.-B.; Yan, P.-F. A series of salen-type asymmetric dinuclear Dy(iii) complexes: site-resolved two-step magnetic relaxation process. *CrystEngComm* **2018**, *20*, 777−786. (f) Huang, Y.; Li, J.-X.; Ge, Y.; Zhang, X.-M.; Xu, Y.; Li, Y.; Zhang, Y.-Q.; Yao, J.-L. Designing asymmetric Dy2 single-molecule magnets with two-step relaxation processes by the modification of the coordination environments of Dy(iii) ions. *Dalton Trans.* **2020**, *49*, 8976−8984. (g) Lyu, D.-P.; Zheng, J.-Y.; Li, Q.-W.; Liu, J.-L.; Chen, Y.-C.; Jia, J.-H.; Tong, M.-L. Construction of lanthanide single-molecule magnets with the "magnetic motif" $[Dy(MQ)_4]^-$. *Inorg. Chem. Front.* **2017**, *4*, 1776−1782.

(41) Antal, P.; Drahoš, B.; Herchel, R.; Trávníček, Z. Muffin-like lanthanide complexes with an N5O2-donor macrocyclic ligand showing field-induced single-molecule magnet behavior. *Dalton Trans.* **2016**, *45*, 15114−15121.

(42) (a) Mandal, L.; Biswas, S.; Cosquer, G.; Shen, Y.; Yamashita, M. Anion-driven structures and SMM behavior of dinuclear terbium and ytterbium complexes. *Dalton Trans.* **2018**, *47*, 17493−17499. (b) Harriman, K. L. M.; Errulat, D.; Murugesu, M. Magnetic Axiality: Design Principles from Molecules to Materials. *Trends in Chem.* **2019**, *1*, 425−439.

(43) (a) Tang, J.; Hewitt, I.; Madhu, N. T.; Chastanet, G.; Wernsdorfer, W.; Anson, C. E.; Benelli, C.; Sessoli, R.; Powell, A. K. Dysprosium Triangles Showing Single-Molecule Magnet Behavior of Thermally Excited Spin States. *Angew. Chem., Int. Ed.* **2006**, *45*, 1729−1733. (b) Marx, R.; Moro, F.; Dörfel, M.; Ungur, L.; Waters, M.; Jiang, S. D.; Orlita, M.; Taylor, J.; Frey, W.; Chibotaru, L. F.; van Slageren, J. Spectroscopic determination of crystal field splittings in lanthanide double deckers. *Chem. Sci.* **2014**, *5*, 3287−3293. (c) Rinehart, J. D.; Long, J. R. Exploiting single-ion anisotropy in the design of f-element single-molecule magnets. *Chem. Sci.* **2011**, *2*, 2078−2085.

(44) Stevens, K. Matrix elements and operator equivalents connected with the magnetic properties of rare earth ions. *Proc. Phys. Soc., London, Sect. A* **1952**, *65*, 209.

(45) Chibotaru, L.; Ungur, L. *Computer Programs SINGLE_ANISO and POLY_ANISO*; University of Leuven, Leuven, Belgium, 2006; p 2.

(46) Boulon, M.-E.; Cucinotta, G.; Luzon, J.; Degl'Innocenti, C.; Perfetti, M.; Bernot, K.; Calvez, G.; Caneschi, A.; Sessoli, R. Magnetic Anisotropy and Spin-Parity Effect Along the Series of Lanthanide Complexes with DOTA. *Angew. Chem., Int. Ed.* **2013**, *52*, 350−354.

(47) Dey, S.; Rajaraman, G. An approach to estimate the barrier height for magnetisation reversal in {Dy2} SMMs using ab initio calculations. *Dalton Trans.* **2020**, *49*, 14781−14785.

https://doi.org/10.1021/acs.inorgchem.1c00249
Inorg. Chem. 2021, 60, 8530−8545